2-1-2014

Ta-W-O nanostructured photoanodes for enhanced solar fuel production: experimental and density functional theory investigation

Ramy Nashed

The American University in Cairo

School of Science and Engineering

Ta-W-O Nanostructured Photoanodes for Enhanced Solar Fuel Production: Experimental and Density Functional Theory Investigation

A Thesis Submitted to

Electrical Engineering department

in partial fulfillment of the requirements

for the degree of Master of Science

by Ramy Nashed

under the supervision of Dr. Yehea Ismail

and co-supervisor Dr. Nageh Allam

October 2013

Cairo, Egypt

Thesis Approval

Dr. Yehea Ismail
Thesis Advisor
Professor
Electronics Engineering Department, School of Sciences and Engineering, American University in Cairo
Signature:.....

Dr. Nageh Allam
Thesis Advisor
Assistant Professor
Physics Department, School of Sciences and Engineering , American University in Cairo
Signature:.....

Dr. Ahmed Abou-Auf
Internal Examiner
Associate Professor
Electronics Engineering Department, School of Sciences and Engineering, American University in Cairo
Signature:.....

Dr. Mohab Anis
Internal Examiner
Associate Professor
Electronics Engineering Department, School of Sciences and Engineering, American University in Cairo
Signature:.....

Dr. Walid Ibrahim
External Examiner
Assistant Professor
Chemistry Department, Cairo University
Signature:.....

Dr. Karim Seddik
Observer
Assistant Professor
Electronics Engineering Department, School of Sciences and Engineering, American University in Cairo
Signature:.....

Abstract

The demand on energy is now increasing at an unprecedented rate due to the high technology revolution. Unfortunately, we can no longer depend on the current energy resources, which is mainly fossil fuels, since they are limited and have dangerous impacts on the environment. Hydrogen has recently received a great attention as an alternative fuel because it is a renewable, clean fuel and its energy content is three times that of gasoline. Photoelectrochemical water splitting is a very attractive method of producing hydrogen due to its simplicity and low cost. However, the semiconductor material used as the photoanode still needs to be optimized.

Ta_2O_5 is considered a very promising semiconductor material for water photolysis as its conduction band minimum and valence band maximum are suitable for water splitting beside being highly stable in aqueous solutions. Unfortunately, the material's bandgap is ~3.9 eV, which limits its absorption spectrum to the ultraviolet region. However, mixing Ta_2O_5 with WO_3 (2.7 eV) is expected to red shifts its absorption to the visible region.

We used Density Functional Theory (DFT) to study the electronic and optical properties of Ta-W-O system. Unfortunately, the reported calculations so far failed to estimate the bandgap with an acceptable accuracy that enables the understanding of the optoelectronic properties of the material. Herein, we proposed a new crystal structure and showed that the use of PBE0 hybrid functional reduced the error in bandgap estimation from 95% to 5% resulting in a calculated bandgap of 3.7 eV. This bridges the gap further between ab-initio DFT calculations and experiments.

Using the proposed structure for Ta_2O_5, we calculated the band structure and the hole effective mass for Ta-W-O system. The bandgap calculations showed a large and composition-

dependent bowing parameter. The electron excitation from the Ta_2O_5 valence band to WO_3 conduction band at high W content may contribute to the pronounced decrease in the conduction band energy. The staggered bandgap type between Ta_2O_5 and WO_3, as revealed from the energy band diagram, resulted in efficient charge carriers separation. The minimum effective mass occurs along the y-direction and decrease monotonically with increasing W content.

Based on the DFT calculations, preliminary experimental work was carried out on low concentration W alloys, namely 2.5% and 10%W. Diffuse reflectance measurements show that the bandgap decreases with increasing W content. This suggests that alloys with high W content are able to harvest a wider range of the solar spectrum and hence higher photo-conversion efficiency. Moreover, XRD analysis showed that the alloys maintained the orthorhombic structure of pristine Ta_2O_5. However, the lattice parameters expanded as the W content increased owing to larger atomic radius of W. Furthermore, XPS analysis asserts the charge transfer model that was drawn from DFT calculations in which the charge carriers are transferred from the valence band of Ta_2O_5 to the conduction band of WO_3. Finally, the photocurrent of 10%W alloy was increased by about 100x compared to pristine Ta_2O_5.

ACKNOWLEDGEMENT

This work would not have been possible without the support and valuable inputs of many people to whom I am really grateful. First of all, I would like to express my deepest gratitude to my parents and my sister for their continuous encouragement and support. They bore a lot especially in my hard moments. It is also a great honor for me to thank Dr Nageh Allam, my co-supervisor, who guided me throughout the development of this thesis and who taught me how to carry out cutting edge research and be part of the research community. He has just been an amazing supervisor. Not forgetting Dr Yehea Ismail, my supervisor, who provided for me a great research environment and didn't hesitate to provide me with all the materials I needed. Additionally, I can't express my thanks to Dr. Mostafa El Sayed, from Georgia Institute of Technology, who hosted me in his lab to conduct the experimental part of this work. Also I would like to thank Dr Faisal Alamgir and Dr Hong Li, from Georgia Institute of Technology, for their fruitful conversations and discussions and their insightful suggestions.

Special thanks shall also go to Dr Walid Hassan who helped me understand Density Functional Theory and guided me throughout the whole computational section. And last but my no means least, I would like to thank all the group members, whether at AUC or at Georgia Institute of Technology, for being such a great company and giving me help whenever I need it.

Publications

1. Nashed, R.; Ismail, Y.; Allam, N. K., Recent advances in the use of density functional theory to design efficient solar energy-based renewable systems. *Journal of Renewable and Sustainable Energy* **2013,** *5* (2). Cited: 3

2. Nashed, R.; Hassan, W. M. I.; Ismail, Y.; Allam, N. K., Unravelling the interplay of crystal structure and electronic band structure of tantalum oxide (Ta_2O_5). *Physical Chemistry Chemical Physics* **2013,** *15* (5), 1352-1357. Cited: 8

3. Nashed, R.; Alamgir, F.M.; Jang, S.S.; Ismail, Y.; ElSayed, M.A.; Allam, N. K., Bandgap Bowing for Efficient Ta-W-O photoanodes: Insights from Density Functional Theory and X-Ray Diffraction. *Appl. Phys. Lett.* **2013**, *103* (13)

4. Nashed, R.; Alamgir, F.M.; Jang, S.S.; Ismail, Y.; ElSayed, M.A.; Allam, N. K., Towards a Perfect System for Solar Hydrogen Production: An Example of Synergy on the Atomic Scale. SPIE International Symposium on Solar Energy+Technology, 25-29 August 2013, San Diego, California, USA

Table of Contents

List of Figures

List of Tables

CHAPTER 1

INTRODUCTION

1.1 Energy Crisis

Mankind needs energy to make to live. Since the Industrial Revolution, humans have used fossil fuels as their primary energy source. As the world becomes more civilized, the demand on energy increases resulting in the depletion of fossil fuel reserves at a much higher rate than in the past. Figure 1.1 shows the consumption of oil and gas, as examples of fossil fuels, over a long period of time [1]. Up to the beginning of the twentieth century, the consumption of reserves was practically negligible. The consumption then rises exponentially to a maximum that will be reached after one or two decades. After reaching that maximum, the consumption will decrease again due to the gradual depletion of the reserves. The reserves which have accumulated over millions of years will be used up over a period of about one hundred years [1].

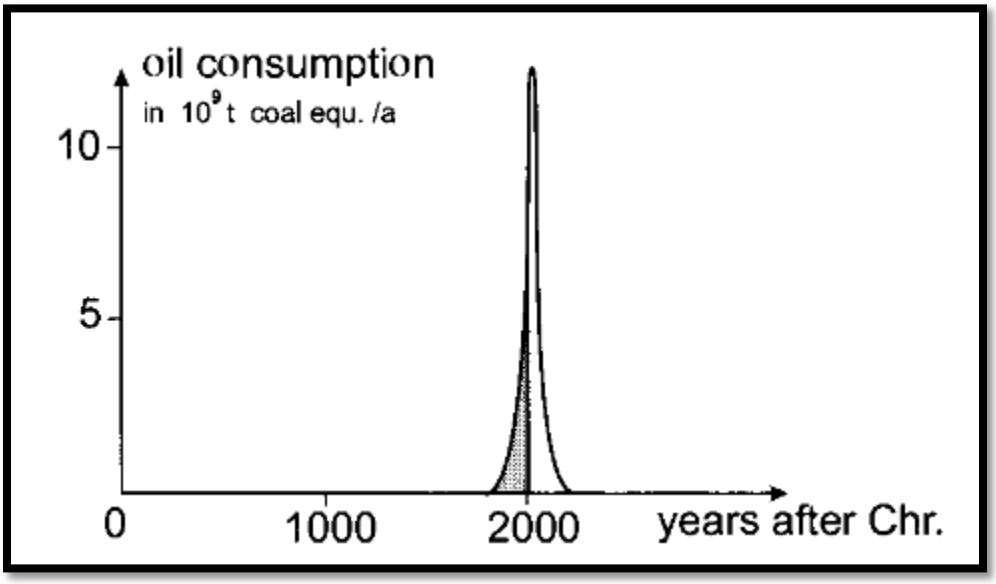

Figure 1.1: Annual consumption of oil. The area under the curve gives the estimated total oil reserves [1].

A more serious problem occurs during the combustion of the fossil fuels. The burning of fossil fuels produces CO_2 gas through the reaction between carbon found in fossil fuels and

oxygen found in the atmosphere. If the rate at which oxygen is produced by plants through photosynthesis is less than the rate at which it is consumed through combustion of fossil fuels, the amount of oxygen in the atmosphere will be reduced; threatening the life on earth. Furthermore, continuing to add carbon dioxide to the atmosphere is projected to lead to significant and persistent changes in climate, including an increase in the average global temperature of 1.4°C to 5.8°C over the course of this century [2]. All tri-atomic molecules, including CO_2, are good absorbers in the infrared region. To keep the temperature of the earth stationary, the solar radiation incident from the sun reaching the surface of the earth should be balanced with the energy emitted by the surface of the earth to outer space. In the presence of CO_2, a great part of the energy emitted by the surface of the earth is absorbed by CO_2 which increases the temperature of the atmosphere and hence heat energy is re-emitted back to the earth. This is known as the green house effect [1]. Figure 1.2 illustrates the relationship between temperature and atmospheric carbon dioxide concentrations over the past 150 years. It is clear that the rise of the global temperature matches with the concentration of carbon dioxide [3, 4].

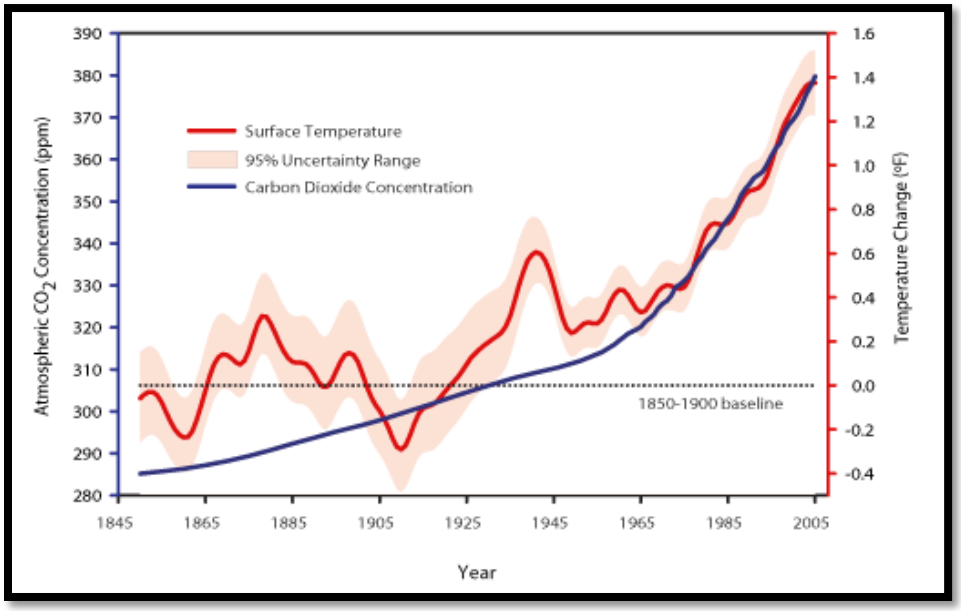

Figure 1.2: The relationship between atmospheric CO_2 concentration and surface temperature for the past 150 years. Source of CO_2 Concentration data: [3], Source of Temperature data: [4]

Increasing the global temperature has worldwide implications including, but not limited to, the melting of glaciers and the rise of sea level. Statistics showed that[2] the maximum surface-melt area on the Greenland Ice Sheet, which dominates land ice in the Arctic, increased on average by 16% from 1979 to 2002, an area roughly the size of Sweden, with considerable variation from year to year. Figure 1.3 compares the melt extent on Greenland in 1992 and 2002 [2]. It is obvious that the rate of melting is rising tremendously. Global average sea level rose by about eight centimeters in the past twenty years and the rate of rise has been increasing. The primary factors contributing to this rise are thermal expansion due to ocean warming and melting of land-based ice that increases the total amount of water in the ocean. Global average sea level is projected to rise 10 to 90 centimeters during this century, with the rate of rise accelerating as the century progresses. Models indicate that warming over Greenland is likely to be of a magnitude that would eventually lead to a virtually complete melting of the Greenland Ice Sheet, with a resulting sea-level rise of about seven meters.

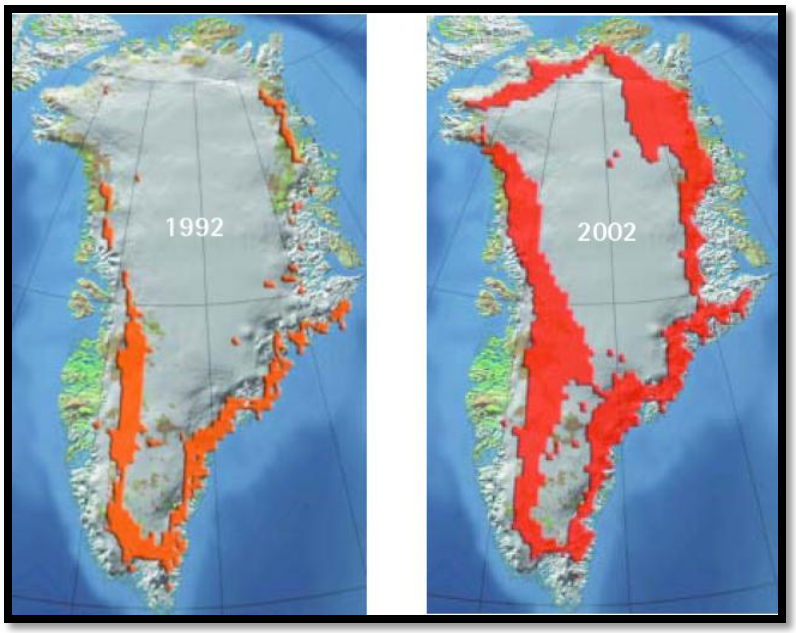

Figure 1.3: Greenland Ice Sheet Melt Extent [2]

Global warming also affects the life of birds and animals. For example, polar bears are unlikely to survive if there is an almost complete loss of summer sea-ice cover, which is projected to occur before the end of this century. The loss of polar bears is likely to have significant and rapid consequences for the ecosystems that they currently occupy. Also, the ice-dependent seals are particularly vulnerable to the observed and projected reductions in arctic sea ice because they give birth to and nurse their pups on the ice and use it as a resting platform. Furthermore, several hundred million birds migrate to the Arctic each summer. Important breeding and nesting areas are projected to decrease sharply as tree line advances northward. A number of bird species, including several globally endangered seabird species, are projected to lose more than 50% of their breeding area during this century [2].

For these reasons, scientists started to look for better energy alternatives that are not harmful to the environment. Solar energy is the most appealing energy source to replace fossil fuel since it is renewable and clean. Furthermore, the amount of solar energy reaching the earth is four orders of magnitude greater than the current world's energy consumption [5]. Unfortunately, solar irradiance is neither constant nor permanent throughout the whole day and so an energy storage medium is required. In this regard, hydrogen is a very promising medium to store solar energy for the following reasons:

1. The energy content per unit mass of hydrogen is three times that of gasoline [6]
2. Upon combustion in air, hydrogen does not emit any green house gases, i.e. environmentally friendly [7].
3. It can be stored in liquid, gaseous, or metal halide forms [7].
4. It can be transported over large distances through pipelines [7].

There are several methods to produce hydrogen. About 95% of the hydrogen produced in the United States is produced via steam-methane reforming method, which involves a reaction between methane and water vapor [7]. Unfortunately, this reaction produces carbon monoxide and carbon dioxide gases as byproducts, which are hazardous to the environment. Producing hydrogen in a clean way is highly desirable in order to obtain a sustainable hydrogen fuel. Towards this end, water splitting by solar energy represents a very attractive avenue to produce hydrogen as it does not involve the production of any harmful gases throughout the whole process of hydrogen production.

1.2 Physics of Water Splitting

Figure 1.4 shows a schematic diagram of the photochemical water splitting system. It consists of an n-type semiconductor that acts as a photoanode and a metal electrode acting as the cathode. When light strikes the photoanode, electrons are excited from the valence band to the conduction band generating an electron-hole pairs. The holes diffuse to the interface between the photoanode and water and combine with oxygen ions in water forming O_2 gas at the anode. The hydrogen ions formed after the oxidation of water will diffuse towards the cathode. At the same time, the excited electrons will flow through the wire to the cathode and combine with hydrogen ions forming hydrogen gas. Likewise, a p-type semiconductor can be used, which in this case acts as a photocathode in combination with a metal anode. However, this setup is less common as most p-type semiconductors are not stable in aqueous solutions.

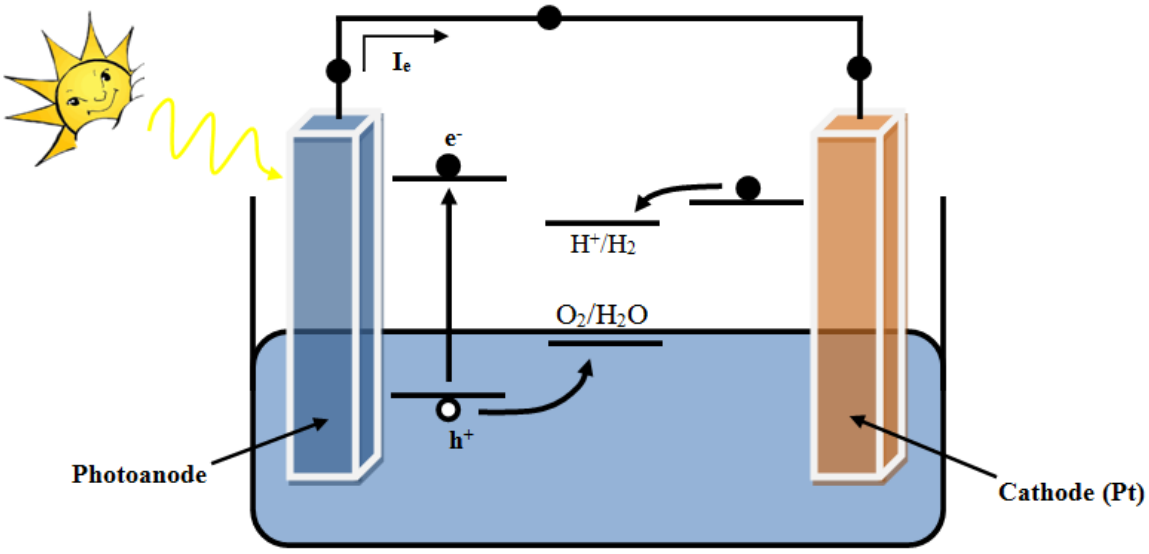

Figure 1.4: Schematic diagram of photoelectrochemical cell

To effectively produce hydrogen, the semiconductor photoanode should fulfill several requirements: (a) the semiconductor should have a bandgap of nearly 2 eV; (b) the position of the conduction band minimum should be more negative than the hydrogen evolution potential and the valence band maximum should be more positive than the oxygen evolution potential; (c) the semiconductor should be relatively stable in aqueous electrolytes [8, 9].

Figure 1.5 illustrates the band diagram of the photoelectrochemical cell [7]. In Figure 1.5a, no contact was yet established between the electrodes and the electrolyte. Upon contact, the photoanode should be in equilibrium with the electrolyte and so electrons flow from the photoanode to the electrolyte leaving a depletion region of positive ions in the photoanode. The positive ions attract negatively charged electrolyte forming a Helmholtz layer. This creates an electric field which, in turn, creates band bending as shown in Figure 1.5b. This electric field acts as a barrier against further flow of electrons to the electrolyte and hence, upon illumination, only holes can flow to the electrolyte whereas the electrons are swept to the bulk and then flow through the wire to the cathode. E_B denotes the height of this barrier which is the difference

between the positions of the conduction band minimum before and after contact with the electrolyte. When the photoanode is illuminated (Figure 1.5c), electron-hole pairs are generated. The generated electrons combine with some of the positive ions in the depletion region and reduce the potential barrier. The holes can drift to the interface between the photoanode and water and produce oxygen, however, the Fermi level of the metal cathode is still below the hydrogen evolution potential and hence hydrogen cannot be produced. This problem is alleviated by adding an external bias, as shown in Figure 1.5d. The bias can either be provided electrically through a voltage source or through direct connection with the output port of a solar cell, hence making the hydrogen production process sustainable.

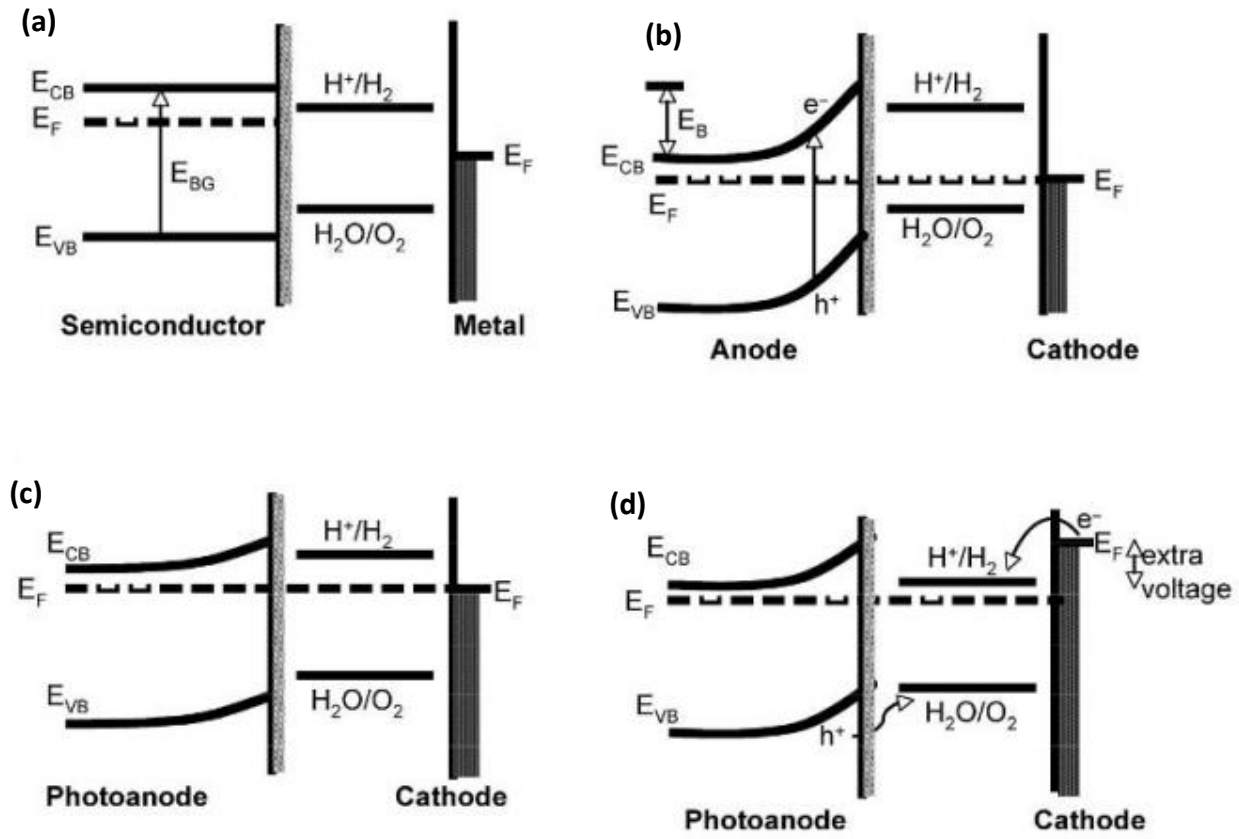

Figure 1.5: Band diagram of a two-electrode photoelectrochemical cell (a) no contact, (b) equilibrium in dark, (c) equilibrium under illumination, (d) illumination under applied bias [7].

Another important issue that arises when designing an efficient photoelectrochemical cell is the stability of the semiconductor electrode. This originates from the photo-generated electron-hole pairs. The generated electrons and holes can reduce or oxidize the semiconductor, respectively, leading to photocorrosion. To address the electrode stability in the electrolyte, Gerischer [10] and Bard [11] developed a simple model in which the electrode stability is represented by a cathodic and anodic redox potentials on an energy band diagram to represent the stability of the electrode when being used as a cathode or an anode, respectively. This is illustrated in Figure 1.6. In order for the semiconductor electrode to be stable as a cathode, the cathodic redox potential should be located above the electrode's conduction band minimum whereas the electrode is considered stable as an anode if its anodic redox potential is below the valence band maximum. Figure 1.6b,c suggest that an electrode can be stable for either oxidation or reduction process. It can also be unstable for both processes as depicted in Figure 1.6c.

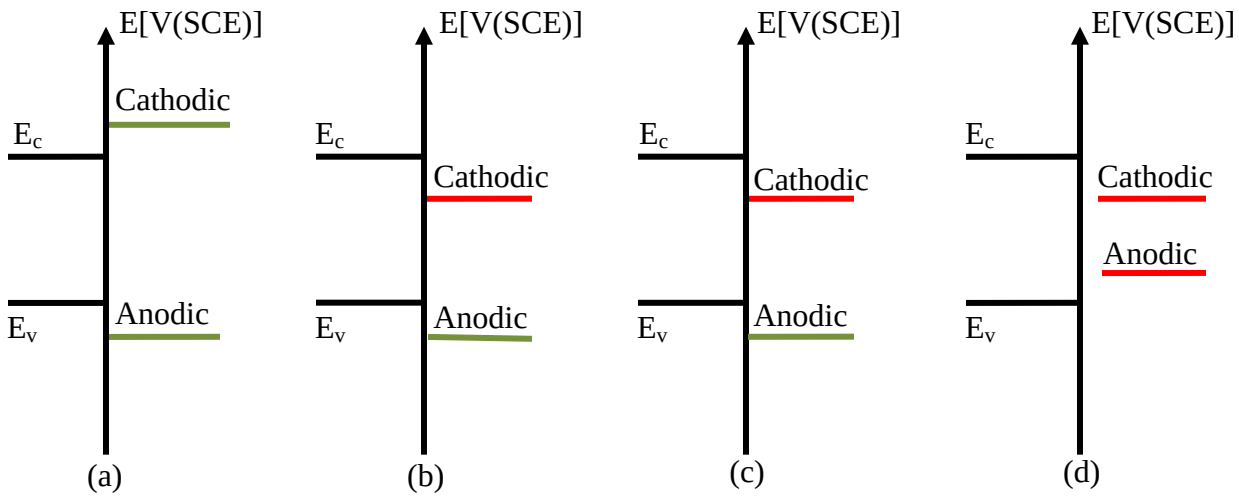

Figure 1.6: Energy level diagrams of a semiconductor in an electrolyte under the conditions of: (a) electrode stability, (b) cathodic decomposition, (c) anodic decomposition, (d) anodic and cathodic decomposition

Nanotechnology can be implemented in photoelectrochemical cells in order to improve its efficiency. Nanoparticle photoanodes can offer higher efficiency owing to the increased surface

to volume ratio, which increases the total active area for the water splitting process. Also, nanoparticles increase the effective optical path of photons by enhancing the scattering and hence leading to better absorption. However, the generated electrons suffer from random walk between the nanoparticles and are subject to potential recombination in the defect states at the grain boundaries between the nanoparticles, Figure 1.7a [12]. Fortunately, nanotubes can overcome this problem by allowing a vectorial charge transfer through the wall thickness of the tubes whereas light absorption occurs along their lengths, as depicted in Figure 1.7b [12]. It is clear that one can design the nanotubes such that they have a wall thickness lower than the diffusion length to minimize charge recombination and at the same time have enough length to increase the light absorption.

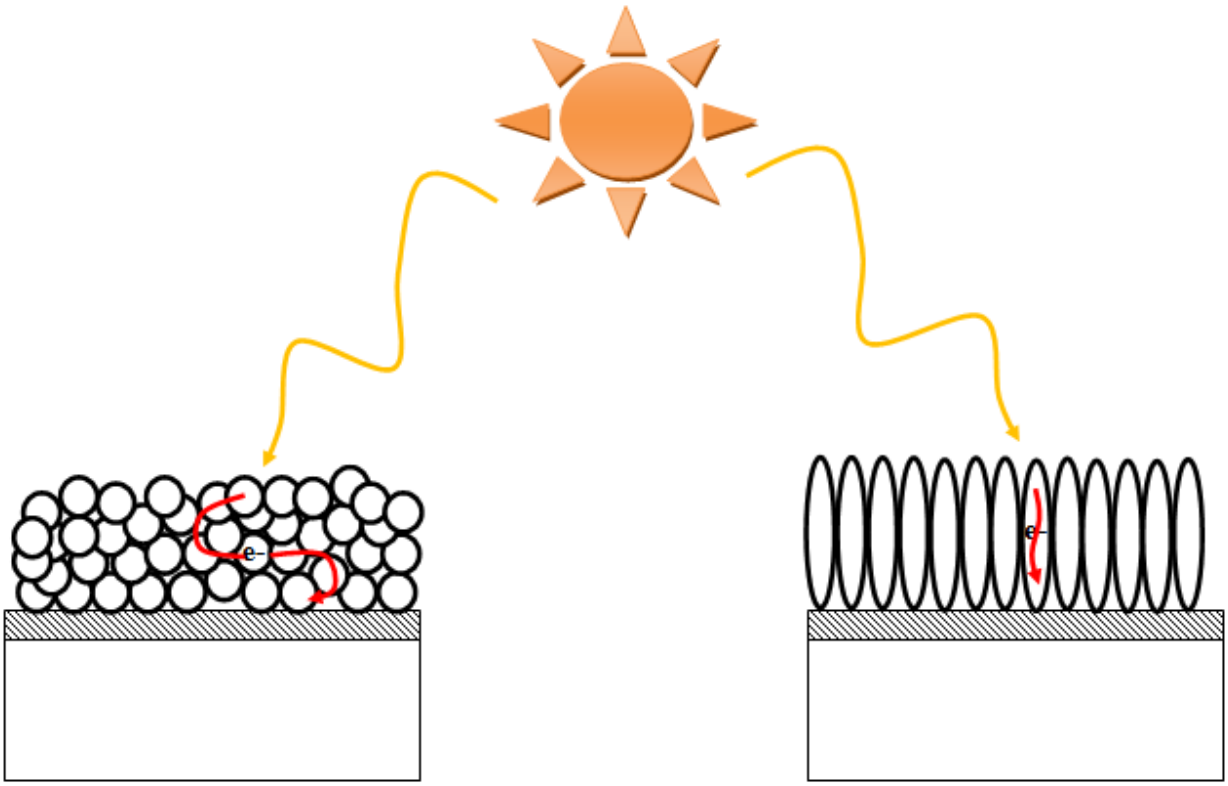

Figure 1.7: Schematic diagram of electron transport through: (a) spherical nanoparticles, (b) nanotubes [12].

1.3 History of Photoanodes

The first demonstration of water splitting was demonstrated by Fujishima and Honda in 1972, using a single crystal TiO_2 electrode[13]. Although TiO_2 is cheap and relatively stable in aqueous solution, the efficiency was very low due to its large energy gap (~3 eV). Since then, a lot of efforts have been exerted in order to discover efficient materials for water splitting. III-V materials can offer very high efficiencies[14]. However, they are not stable in water besides being very expensive. Several metal oxides have also been investigated in search for a more efficient photoelectrochemical water splitting process[12, 15-20]. However, none of the investigated semiconductors simultaneously satisfy all the three criteria required for water splitting by solar energy. Therefore, new materials are still to be discovered and designed.

Towards this end, scientists tried to mix materials together, in an attempt to arrive at a new material with enhanced photocatalytic activity. For example, Park et al.[21] and Asahi et al.[22] studied the effect of doping TiO_2 with nonmetals, namely carbon and nitrogen, respectively. They found that upon doping, the absorption spectrum of TiO_2 is extended into the visible region. Also, there have been some attempts to dope TiO_2 with transitional metals[23] or even to use mixed metal oxides[24, 25]. These studies showed similar results as nonmetal dopants. However, the overall efficiency remained low. Beside TiO_2, other metal oxides have been studied. For instance, doping WO_3 with other metals such as Ti[26], V[27], and Cu[28] has been considered with a reported enhancement in photocatalytic activity upon doping. The main goal of these studies was to reduce the bandgap of WO_3 and hence widens its absorption spectrum. Unfortunately, even a wide absorption does not guarantee an efficient water splitting process since the conduction band edge of WO_3 lies below the hydrogen evolution potential by 0.4 eV[29, 30] and hence an external bias is required to split water. More interestingly, for V-doped WO3, the bandgap initially increases from 3.16 eV to 3.28 eV for V/W of 0.003 then it decreases back to 3.15 eV at V/W of 0.047[31]. A similar phenomenon occurs on doping $BiVO_4$ with W and Mo in which the bandgap remained unchanged after doping [32]. The enhancement in the photocatalytic activity for that system is believed to be due to the better separation of the photo-generated electron-hair pair [32].

1.4 Density Functional Theory

The above discussion shows that different dopants have different effects on materials and hence a systematic approach is required to better understand these effects. Also, in order to design an efficient material for water splitting, the structure, optical, and electrical properties of the

material has to be carefully studied. Density Functional Theory (DFT) is a very powerful tool towards this end. In this section we discuss the basics of DFT and show how it can be used to design efficient photoanodes for water splitting cells.

1.4.1 Pre-DFT attempts

The physical and chemical properties of any system can be determined exactly by solving the many-body Schrodinger equation:

$$\hat{H}\Psi_i(r,R) = E_i\Psi_i(r,R) \tag{1.1}$$

where Ψ_i is the wave function of the system, E_i is the eigen-values, which are the allowed energy states produced by solving (1.1), and $\hat{H}$ is the Hamiltonian operator. For interacting atoms, $\hat{H}$ is defined as [33]:

$$\hat{H} = -\sum_{I=1}^{P}\frac{\hbar^2}{2M_I}\nabla_I^2 - \sum_{i=1}^{N}\frac{\hbar^2}{2m}\nabla_i^2 + \frac{e^2}{2}\sum_{I=1}^{P}\sum_{J\neq I}^{P}\frac{Z_I Z_J}{|R_I - R_J|} + \frac{e^2}{2}\sum_{i=1}^{N}\sum_{j\neq i}^{N}\frac{1}{|r_I - r_J|} - e^2\sum_{I=1}^{P}\sum_{i=1}^{N}\frac{Z_I}{|R_I - r_i|} \tag{1.2}$$

where $R = \{R_I\}$, $I = 1, \ldots, P$, is a set of P nuclear coordinates and $r = \{r_i\}$, $i = 1, \ldots, N$, is a set of N electronic coordinates. Z_I and M_I are the P nuclear charges and masses, respectively. When interpreted physically, the first term on the right hand side of (1.2) is the kinetic energy of the P nuclei, the second term is the kinetic energy of the N electrons, the third term is the Coulomb repulsive potential between each pair of nuclei, the fourth term is the Coulomb repulsive potential between each pair of electrons, and the fifth term is the Coulomb attraction potential between the electrons and the nuclei in the system.

It is obvious that the Hamiltonian for such systems is very complicated and requires large computational effort especially for large atoms and molecules. Also, the analytical expression for

the many-electron Hamiltonian is not known. For these reasons, various simplifications have been introduced to (1.2). The first approximation is the Born-Oppenheimer approximation [34] which is based on neglecting the kinetic energy of nuclei and treating their repulsive potential as a constant. The plausibility of this approximation is due to the fact that the mass of the nuclei is much greater than that of the electrons and thus the nuclei can be assumed stationary with respect to the electrons. This gives rise to the so-called electronic Hamiltonian:

$$\hat{H}_{elec} = -\sum_{i=1}^{N} \frac{\hbar^2}{2m} \nabla_i^2 + \frac{e^2}{2} \sum_{i=1}^{N} \sum_{j \neq i}^{N} \frac{1}{|r_I - r_J|} - e^2 \sum_{I=1}^{P} \sum_{i=1}^{N} \frac{Z_I}{|\mathrm{R}_I - r_i|} \tag{1.3}$$

The electronic energy, E_{elec}, can be found by substituting (1.3) in (1.1). The total energy can then be calculated by adding E_{elec} to the constant nuclear repulsion term E_{nuc}:

$$E_{nuc} = \frac{e^2}{2} \sum_{I=1}^{P} \sum_{J \neq I}^{P} \frac{Z_I Z_J}{|\mathrm{R}_I - \mathrm{R}_J|} \tag{1.4}$$

Although the Hamiltonian was greatly simplified by the Born-Oppenheimer approximation, the second term in (1.3) still represents a computational problem as it involves pair-wise Coulombic correlation between electrons and hence it is required to consider the contribution of two electrons every time we write the wave function. This renders the wavefunction complicated and the solution of Schrodinger equation hard. Hartree proposed a solution to this problem by assuming that each electron in the system feels an average potential energy due to the other electrons [35]. This allows for treating a single electron at a time and consequently to express the wave function as a product of one-electron wave functions. It uses separation of variables to solve Schrodinger equation, which greatly simplifies the calculations. To determine the expressions for the one-electron wave functions, Hartree and Fock introduced a method which took into account Pauli Exclusion Principle where the many-electron wave function is

approximated by a product of anti-symmetrical one-electron wave functions in the form of a Slater determinant [33]:

$$\Psi_{HF} = \begin{vmatrix} \psi_1(\mathbf{r}_1,\sigma_1) & \psi_1(\mathbf{r}_2,\sigma_2) & \dots & \psi_1(\mathbf{r}_N,\sigma_N) \\ \psi_2(\mathbf{r}_1,\sigma_1) & \psi_2(\mathbf{r}_2,\sigma_2) & \dots & \psi_2(\mathbf{r}_N,\sigma_N) \\ \vdots & \vdots & \ddots & \vdots \\ \psi_N(\mathbf{r}_1,\sigma_1) & \psi_N(\mathbf{r}_2,\sigma_2) & \dots & \psi_N(\mathbf{r}_N,\sigma_N) \end{vmatrix} \tag{1.5}$$

where $\mathbf{r}_i$ signifies the spatial position of the electron i and σ signifies its spin. $\Psi_i(\mathbf{r}_i, \sigma_i)$ are expressed as a Linear Combinations of Atomic Orbitals (LCAO) to form Molecular Orbitals (MO). Using this approximation, the energy of the system can be calculated as:

$$E_{HF} = \sum_{i=1}^{N} H_i + \frac{1}{2} \sum_{i,j=1}^{N} (J_{ij} - K_{ij}) \tag{1.6}$$

where H_i represents the kinetic energy and the electron-nucleus Coulomb attraction, J_{ij} are the coulomb integrals, which represent the repulsive potential that the electron feels due to an average distribution of the rest of the electrons, and K_{ij} is the exchange integrals that are a quantum mechanical effect occurring due to the overlapping of orbitals, which combines all possible permutations of electron energy distribution in the system. This approximation is called Hartree-Fock (HF) or Self-Consistent Field (SCF) approximation and it includes particle exchange in an exact manner [36, 37]. The main drawback of this method is that the computational effort needed to compute (1.5) scales by M^3, where M is the number of atomic orbitals.

1.4.2 Development of DFT

Despite the different approximations applied to the Hamiltonian and the wave function, solving Schrodinger equation remains very hard and nearly impossible for large atoms and molecules

since the wave function is a function of 3N variables, where N is the number of electrons in the system. Density Functional Theory solved this problem by reducing the number of variables to three variables only [38]. This is because DFT is based on using the electron density, which is a function of the three spatial coordinates, to calculate the energy of the system. This considerably reduced the computational cost and allowed for determining the physical and chemical properties of large atoms and molecules.

The efforts of Thomas [39] and Fermi [40], which dates back to 1927, represent the seed of the DFT. In Thomas-Fermi model, the energy of the system is calculated in terms of the electron density as:

$$E_{TF}[\rho(\mathbf{r})] = \frac{3}{10}(3\pi^2)^{2/3}\int \rho^{5/3}(\mathbf{r})d\mathbf{r} - Z\int \frac{\rho(\mathbf{r})}{r}d\mathbf{r} + \frac{1}{2}\iint \frac{\rho(\mathbf{r}_1)\rho(\mathbf{r}_2)}{r_{12}}d\mathbf{r}_1 d\mathbf{r}_2 \qquad (1.7)$$

where ρ is the electron density. The first term in (1.7) represents the kinetic energy of electrons, the second term is the nuclear attraction between nuclei and electrons, and the third term is the Coulomb repulsion between electrons. The kinetic energy term is found by solving a particle in a box problem assuming a constant electron density. This is a very crude approximation since the electron density is non-uniform and is actually rapidly changing near the nuclei. Also, the exchange and correlation effects are neglected [33]. In 1930, Dirac used the uniform electron density approximation to introduce an expression for the exchange energy [41], which gave rise to Thomas-Fermi-Dirac theory [42]. Weizsacker [43, 44] was the first to target the non-uniform electron density problem in 1935 by providing an expression for the kinetic energy of electrons that depends on the gradient of the electron density in the neighborhood. Considering the gradient of electron density allowed for adding information about how the electron density

changes in the vicinity of each point in space. This led to two refinements to the Thomas-Fermi theory: (1) Thomas-Fermi-Weizsacker theory [44], which corrects the kinetic energy term in Thomas-Fermi theory by considering non-uniform electron density but did not consider exchange correlation energy, (2) Thomas-Fermi-Dirac-Weizsacker [44] which not only corrects the kinetic energy term in Thomas-Fermi but also included the exchange energy term using Dirac approximation. However, this theory is still not accurate as it is based on Dirac approximation.

DFT started to attract great attention after the work done by Hohenberg and Kohn in 1964 who proved that the potential is a unique functional of electron density [38]. This is a marvelous achievement because it means that for each electron density distribution, there is one and only one expression for the energy of the system. The proof of this theorem comes from the fact that, in order to determine the Hamiltonian operator, one needs to determine the number of electrons in the system as well as the positions of the nuclei. The electron density is very powerful in this aspect as the integration of the electron density over the whole space gives the number of electrons and the positions of the cusps found when plotting the electron density versus position represent the locations of the nuclei. According to Hohenberg-Kohn theorem, the energy of the system can be expressed as [38]:

$$E = \int v(\mathbf{r})\rho(\mathbf{r})dr + \frac{1}{2}\iint \frac{\rho(\mathbf{r})\rho(\mathbf{r}')}{|\mathbf{r}-\mathbf{r}'|} d\mathbf{r}d\mathbf{r}' + G[\rho] \tag{1.8}$$

where $v(\mathbf{r})$ represents the nuclear potential. The first term represents the nuclear Coulomb attraction, the second term is the electron Coulomb repulsion and $G[\rho]$ is the sum of the electron kinetic energy, $T[\rho]$, and the exchange and correlation energy [38], $E_{xc}[\rho]$:

$$G[\rho] = T[\rho] + E_{xc}[\rho] \tag{1.9}$$

In their original paper, Hohenberg and Kohn did not propose explicit forms to the kinetic energy and exchange and correlation energies. Kohn and Sham addressed this problem in 1965 [45], shortly after the publication of the original Hohenberg-Kohn theorem. Kohn and Sham provided an exact expression for $T[\rho]$ as well as a semi-exact expression for $E_{xc}[\rho]$. The calculation of the $E_{xc}[\rho]$ term depends on splitting it into two terms: Exchange term, E_x, and Correlation term, E_c where E_x is calculated exactly from Hartree-Fock equations and E_c is approximated under the assumption of a uniform electron density. Although the calculation of $E_{xc}[\rho]$ is very accurate, it requires large computational power since the calculation of E_x is based on Hartree-Fock equations, which involve wave functions instead of electron density. For this reason, a simpler expression for $E_{xc}[\rho]$ is suggested by Kohn and Sham assuming uniform electron density for the whole expression of $E_{xc}[\rho]$. From the above discussion, it is obvious that the main challenge in DFT is to find the proper expression for $T[\rho]$ and $E_{xc}[\rho]$.

1.4.3 Basis Sets

The Kohn-Sham equation, which is analogous to Schrodinger equation, can be written as [45]:

$$\left\{-\frac{1}{2}\nabla^2+\left[v(\mathbf{r})+\int\frac{\rho(\mathbf{r}')}{|\mathbf{r}-\mathbf{r}'|}d\mathbf{r}'\right]+\mu_{xc}\left[\rho(\mathbf{r})\right]\right\}\psi_i(\mathbf{r})=\varepsilon_i\psi_i(\mathbf{r}) \tag{1.10}$$

where $v(\mathbf{r})$ is the attractive Coulomb potential between the electron and the nuclei, $\mu_{xc}(\mathbf{r})$ is the density of E_{xc} with respect to ρ, and $\psi_i(\mathbf{r})$ is the Kohn-Sham orbitals which are analogous to wave functions in Schrodinger equation. The numerical solution of (1.10) requires expanding Kohn-Sham orbitals in a set of pseudopotentials [46].

The main types of basis functions are the Slater-Type Orbitals (STOs), Gaussian-Type Orbitals (GTOs), Contracted Gaussian Functions (CGFs), and PseudoPotentials (PPs). Slater-Type Orbitals [47] are functions which decay exponentially far from the origin. They closely resemble the true behavior of atomic wave functions as they have cusps at the nuclei positions. However, they require large computational efforts. On the other hand, Gaussian-Type Orbitals [48] are not as accurate as STOs but they are easier to handle numerically since the product of two GTOs located at different atoms is another GTO located between the atoms, whereas the product of two STOs does not lead to an STO [46]. Contracted Gaussian Functions [48] represent a compromise between the accuracy of STO and the simplicity of GTO where CGF is constructed by approximating STO by a small number of GTOs. PseudoPotentials represent the most attractive basis functions for systems with large number of electrons [46]. The idea of using PseudoPotentials is based on the fact that the binding energy of solids and molecules is dominated by the valence electrons of each atom and hence only the valence electrons need to be considered in (10), which tremendously reduce the number of electrons treated explicitly. This allows for performing DFT calculations on large systems.

1.4.4 DFT Functionals

As mentioned above, the main challenge in DFT is to find the proper expression for $T[\rho]$ and $E_{xc}[\rho]$. Several expressions have been proposed which are briefly described in this section.

1.4.4.1 Local Density Approximation (LDA)

LDA is the first and simplest approximation in DFT. It is based on decomposing the real problem of a non-uniform interacting system into two simpler components: a spatially non-

uniform non-interacting system to calculate $T[\rho]$, and a uniform interacting system to calculate $E_{xc}[\rho]$ [34]. The expression of $E_{xc}[\rho]$ follows that proposed by Kohn and Sham [45]:

$$E_{xc}[\rho] = \int \rho(\mathrm{r})\varepsilon_{xc}[\rho(\mathrm{r})]d\mathrm{r} \tag{1.11}$$

where $\varepsilon_{xc}[\rho]$ is the exchange and correlation energy per electron of a uniform electron gas. In LDA, $\varepsilon_{xc}[\rho]$ is decomposed, like in Kohn-Sham, into two functional: exchange functional (ε_x) and correlation functional (ε_c). The exchange functional is calculated from Dirac's form [49] while the correlation function is unknown and has been simulated in numerical quantum Monte Carlo calculations assuming uniform electron density and yielded nearly exact results [50]. In LDA, $E_{xc}[\rho]$ is very-well approximated since the errors in ε_c tend to be cancelled by ε_x [46].

1.4.4.2 Generalized Gradient Approximation

GGA builds on LDA by considering non-uniform distribution of electrons. In GGA, ε_{xc} is a functional of electron density as well as its gradient which helps to take into account the way by which the electron density changes in the vicinity of the point of interest. This is very crucial when considering points near the nuclei in which the electron density is strongly changing. Nowadays, the most popular GGA in physics is PBE which was proposed by Perdew, Burke, and Ernzerhof in 1996 [51] whereas BLYP, which is a combination of Becke's exchange energy [52] with Lee's, Yang's, and Parr's correlation energy [53], is the most popular GGA in chemistry [46].

1.4.4.3 Meta GGA

Although GAA has shown great improvements in calculations compared to LDA, the chemical accuracy, which requires that the errors in calculations should exceed 1kcal/mol, was not reached

yet [46]. For this reason, several beyond-GGA functionals were introduced. Meta-GGA [54, 55] is an example of beyond-GGA development in which the exchange energy depends on the Laplacian of the spin density, $\nabla^2\rho$, or the local kinetic energy density, τ. The incorporation of Meta-GGA helped to solve some problems of the previous functional such as self-interaction problem in the correlation functional, increasing the accuracy of calculating the exchange functional by recovering the fourth order gradient expansion for slowly varying densities, and obtaining a finite exchange potential at the nucleus [56].

1.4.4.4 Hybrid Functionals

Although LDA and GGA give good approximations for many calculations, they tend to underestimate the transition energy. This is because they don't contain the correct 1/R dependence (where R is the distance between charges) in the exchange functional expression. Hybrid functionals can remedy this problem through the incorporation of the exact Hartree-Fock exchange functional.

Hybrid functionals are based on the exact adiabatic approach [57], which allows for the exact representation of the exchange and correlation energy functional as:

$$E_{xc}[\rho] = \frac{1}{2}\int d\mathrm{r}d\mathrm{r}' \int_{\lambda=0}^{1} d\lambda \frac{\lambda e^2}{|\mathrm{r}-\mathrm{r}'|}\left[<\rho(\mathrm{r})\rho(\mathrm{r}')>_{\rho,\lambda} - \rho(\mathrm{r})\delta(\mathrm{r}-\mathrm{r}')\right] \tag{1.12}$$

where λ is a coupling constant with λ=0 corresponding to non-interacting system and λ=1 corresponding to fully interacting system. A non-interacting system is well-represented by Hartree-Fock equations while GGA is a good representation for a fully-interacting system with a uniform electron density. A logical approximation to the integral in (12) is to consider the extreme cases with λ=0 and λ=1 and use a weighted average to approximate $E_{xc}[\rho]$. Becke's hybrid functional [58], B3, employs this idea and is considered the most successful exchange

functional for chemical applications, especially when combined with LYP GGA [53] functional for E_c to form B3LYP functional which is the most popular functional in quantum chemistry [46].

1.5 Why Ta-W-O System?

Ta_2O_5 is considered a very promising semiconductor material for water photolysis as its conduction band minimum and valence band maximum are suitable for water splitting, as shown in Figure 1.8. Furthermore, Ta_2O_5 is highly stable in aqueous solutions. Unfortunately, the material's bandgap is~3.9 eV, which limits its absorption spectrum to the ultraviolet region (only 3-5% of the solar spectrum). However, doping Ta_2O_5 with the suitable material would extend its absorption to the visible region (~45% of the solar spectrum), hence enhancing its photocatalytic activity. For example, doping Ta_2O_5 with W is expected to red shift its absorption to the visible region as the bandgap of WO_3 is 2.7 eV. Also, doping Ta_2O_5 with 5d materials, such as W, should guarantee high carrier mobility due to the relatively higher delocalization of 5d orbitals compared to its 3d and 4d counterparts. Note that using pristine WO_3 is unfavorable for water photolysis as its conduction band minimum is 0.4 eV more positive than hydrogen evolution potential (See Figure 1.8).

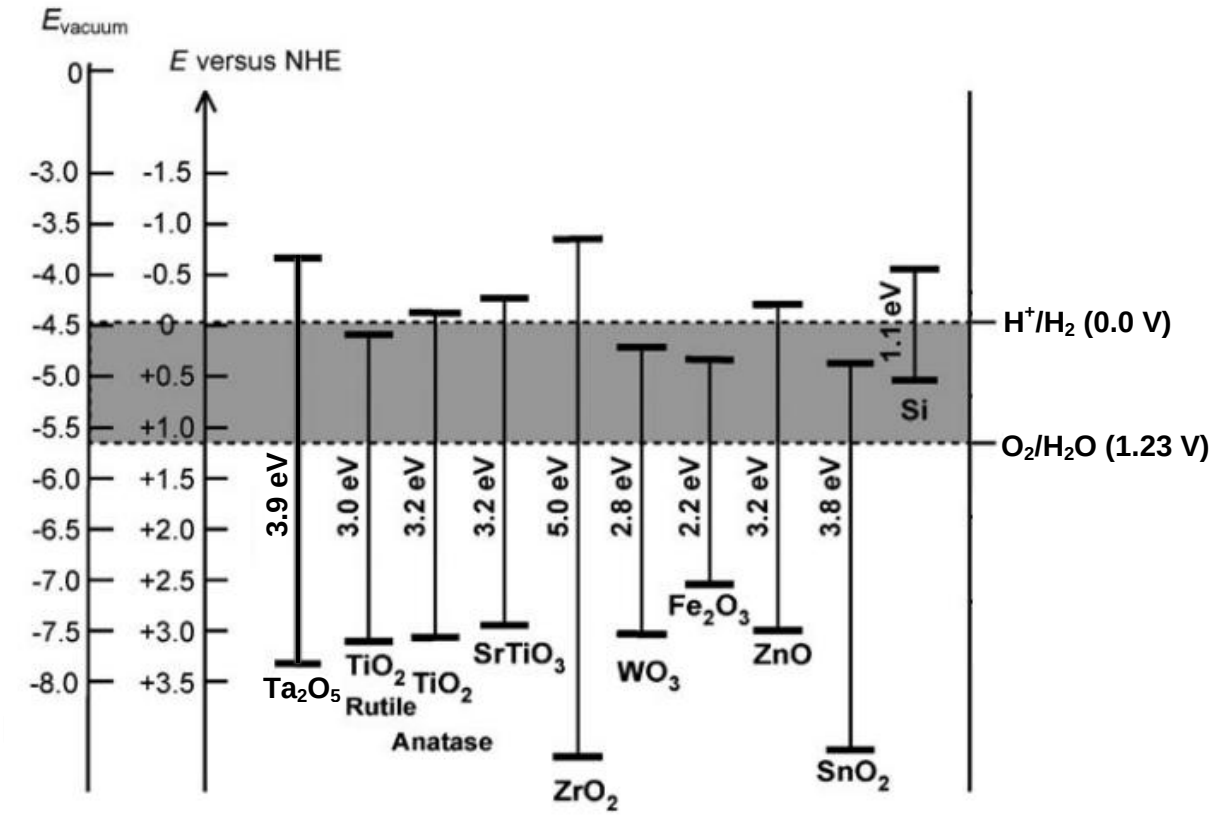

Figure 1.8: Band positions of common semiconductors at pH 0. Redox couples of interest for water purification are shown on the right. The shaded area represents O_2(g) and H_2(g) generating potentials [59].

In fact, Ta-W-O system represents an attractive solution towards a highly efficient photoanode in photoelectrochemical cells owing to the staggered bandgap between Ta_2O_5 and WO_3. Most of the mixed metal oxides proposed to date have a straddling bandgap which enhances recombination, leading to a low photoconversion efficiency. For example, Ti-Fe-O has been extensively studied and was expected to have a high efficiency by combining the good photocorrosion and charge transport properties of TiO_2 with the wide absorption spectrum of Fe_2O_3. However, when such system was tested, it only gave an efficiency of 1.2% at 0.7 V bias [24]. The reason behind such low efficiency can be understood from Figure 1.9(a), where the bandgap of TiO_2 brackets that of Fe_2O_3. Upon illumination, an electron is excited from the valence band of Fe_2O_3 to its conduction band. Due to the band bending, the excited electrons are imposed to move leftwards

where they get trapped. The trapped electrons will then recombine with a photogenerated hole and hence the total current in the system decreases. To assess the efficiency of the Ta-W-O system, we compare it to the Ti-Fe-O system, see Figure 1.9(b). The position of the CBM of WO_3 occurs in the bandgap of Ta_2O_5. Therefore, upon illumination, an electron may be excited from the valence band of Ta_2O_5 to the conduction band of WO_3 and hence decreasing the energy required for the electron excitation. Figure 5b also shows that there is an energy barrier for both holes and electrons, imposing holes and electrons to move in opposite directions and hence maximizing the total current. Based on this comparison, Ta-W-O may be considered as an efficient alternative photoanode material in water splitting systems.

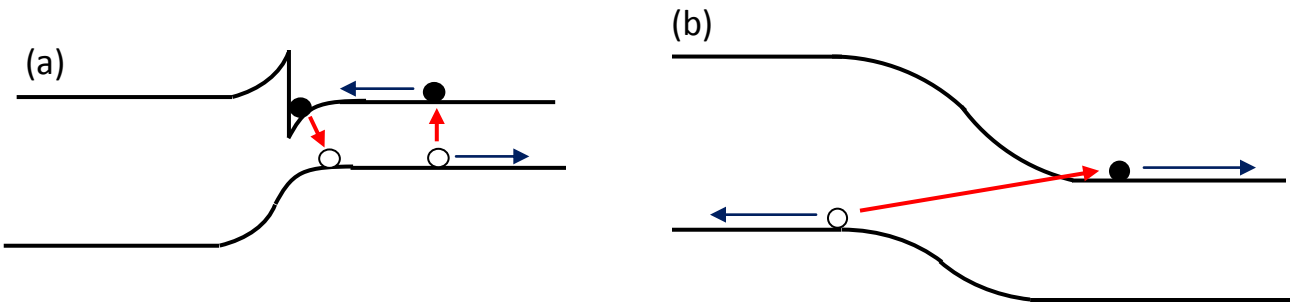

Figure 1.9: Energy band diagrams of (a) Ti-Fe-O and (b) Ta-W-O illustrating the charge carrier transport for both systems

The work in this thesis is classified into two main sections. In the first section we study the effect of W doping on the optical and electrical properties of Ta_2O_5 using density functional theory. Based on the suggestions from density functional theory, we synthesize and characterize the efficiency Ta-W-O alloy as a photoanode in the photoelectrochemical cells. This comprises section two.

CHAPTER 2

MATERIALS AND METHODS

2.1 DFT Calculations

All the calculations for band structure and effective mass for pristine and W-doped Ta_2O_5 were done using CASTEP package in Materials Studio with plane wave basis sets. The crystal structure for Ta_2O_5 was taken from our previous work in Ref. [60]. PBE0 hybrid functional as well as GGA-PBE were used in all calculations. A 1x1x2 and a 1x2x3 super cells were constructed in which one Ta atom was replaced by a W atom to account for 8.3% and 25% doping, respectively. A kinetic energy cut-off of 520 eV was employed for all PBE0 calculations, whereas an energy cut-off of 380 eV was employed for GGA-PBE calculation. Different Monkhorst–Pack[61] k-point grids were used according to the size of the cell to make the calculations reasonably accurate without being computationally costly. For pristine Ta_2O_5 and 50% W doping unit cells, a 2×3×3 k-point grid was utilized. A 2×3×2 and 2×2×1 k-point grids were used for the 25% W and 8.3% W, respectively. Norm conserving[62] and ultrasoft pseudopotentials[63] were used to approximate the core electrons.

2.2 Potentiostatic Anodization

The anodization process was carried out in a two-electrode system with the material to be anodized as the anode and platinum foil as the cathode. Anodization was carried out in an electrolyte of concentrated HF (48% conc.) and H_2SO_4 (96%) mixture which were purchased from J. T. Baker and BDH Chemicals respectively. Agilent E3612A D C power supply was

used to supply the required voltage. The anodization setup is shown in Figure 2.1.

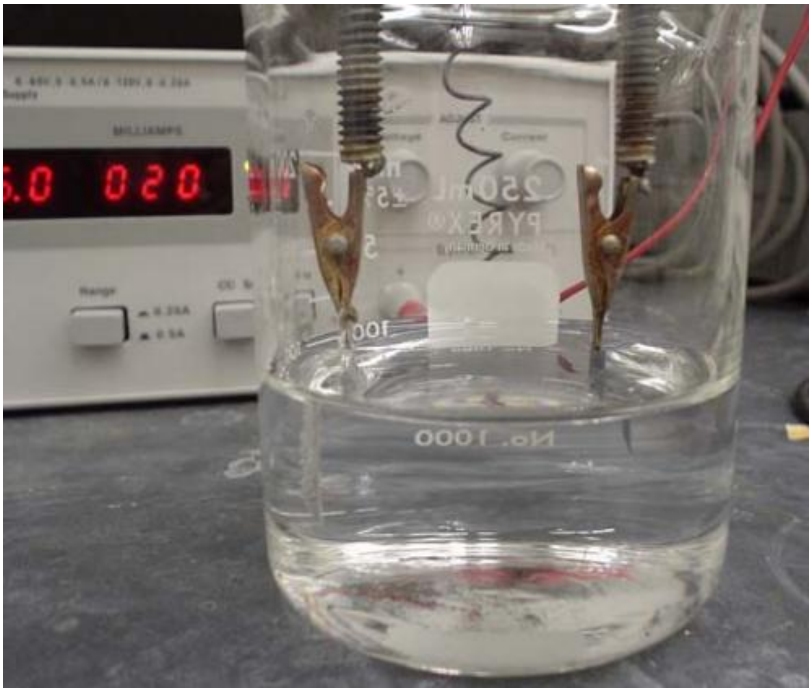

Figure 2.1: Potentiostatic anodization setup

2.2 Scanning Electron Microscopy

The surface structure was examined using Zeiss Ulta-60 Field Emission Scanning Electron Microscope. Because the pore size was very small, sometimes around 30 nm, the working distance was always kept at a height less than 8 mm. For that reason, the InLens detector was generally used since it is placed at an appropriate angle from the sample stage. Using the SE2 detector would not allow for high resolution images at small working distances since the angle between the SE2 detector and the sample stage is very acute and hence the signal arriving to the SE2 detector would be negligibly small. SE2 detector in this case can only be used in smaller magnifications at higher working distances. The Extra High Tension (EHT) was kept below 10 keV to prevent charging of the samples due to its relatively low conductivity.

2.3 Thermal Annealing

A muffle furnace was used to anneal the fabricated nanotubes so as to crystallize the structure. The furnace's temperature was elevated from room temperature to 450 °C at a rate of 1°C/minute. The temperature is then soaked for 4 (or 9) hours then allowed to cool back to the room temperature at the same rate.

2.4 X-Ray Diffraction (XRD)

The XRD analysis was performed on Alpha-1 Panalytical XRD instrument with a CuKα radiation at λ=1.540598A°. The X-Ray tube remains fixed and the sample stage and the detector rotate at an angle of θ and 2θ respectively keeping the angle between the sample and the detector at θ. The scan range was between 20° and 80° with a step size of 0.004° and a time per step of 8.255 seconds. To allow for this scan range, a divergence slit of 0.5° and an anti-scattering slit of 1° were used. A soller slit was used in front of the incident beam to limit its axial (vertical/out-of-plane) divergence.

2.5 X-Ray Photo-electron Spectroscopy (XPS)

Compositional analysis was carried out on Thermo K-alpha XPS instrument with an Al anode. A point size of diameter 200 μm was specified on each sample to carry out the XPS analysis on it. Ni was used a reference since it has a sharp drop-off at the Fermi level.

2.6 Optical and Photoelectrochemical Characterization

The UV-Vis diffuse reflectance measurements were carried out on a Schimadzu UV-VIS spectrophotometer with a solid sample holder. A glass disk was used as a reference which corresponds to 100% reflectance.

The photoelectrochemical characterization is done using three-electrode setup in which the metal oxide nanotubes act as the working electrode, Pt foil acting as the counter electrode, and a Ag/AgCl as the reference electrode. The I-V curve was measured using a CHI760 potentiostat in which the voltage ranges between -1 V and +1 V with a scan rate of 10 mV/s. Sun light was simulated using a 300 Watt Xenon lamp and an Oriel AM1.5 filter. The light intensity was adjusted to 100 mW/cm^2 using an NREL-calibrated silicon solar cell.

CHAPTER 3

DENSITY FUNCTIONAL THEORY STUDY OF TA-W-O SYSTEM

Several polymorphs have been reported for Ta_2O_5 which can be divided into low-temperature (L-Ta_2O_5) and high-temperature (H-Ta_2O_5) Ta_2O_5. The most common polymorphs in L-Ta_2O_5 are β-Ta_2O_5 and δ-Ta_2O_5. Early experiments by Stephenson *et al*. reported an orthorhombic β-Ta_2O_5 with 22 Ta atoms and 55 O atoms [64]. Aleshina and Loginova pointed out later that the data on β-Ta_2O_5 are contradictory and proposed a new orthorhombic structure, which consists of four Ta atoms and ten O atoms [65]. A hexagonal structure (δ-Ta_2O_5) has been observed for Ta_2O_5 films prepared by chemical vapor deposition [66] and magnetron sputtering [67]. However, the calculated density [68] is twice the experimentally reported value [69]. Based on the extinction rule, Fukomoto and Miwa [70] suggested one of the lattice constants should be twice that of the measured value in order to agree with the measured density. Using density functional theory (DFT), it was shown that δ-Ta_2O_5 is more stable than β-Ta_2O_5 by 0.8 eV/cell [71, 72]. More interestingly, a recent study showed that both β- and δ- phases show some instability and that large supercells should be used in calculations to optimize the structure [73]. As was the case with L-Ta_2O_5, orthorhombic [74], tetragonal [75], and monoclinic [76] crystal structures were reported for H-Ta_2O_5. In this work we focus our study on β- and δ-Ta_2O_5 whose crystal structures are shown in Figure 3.1.

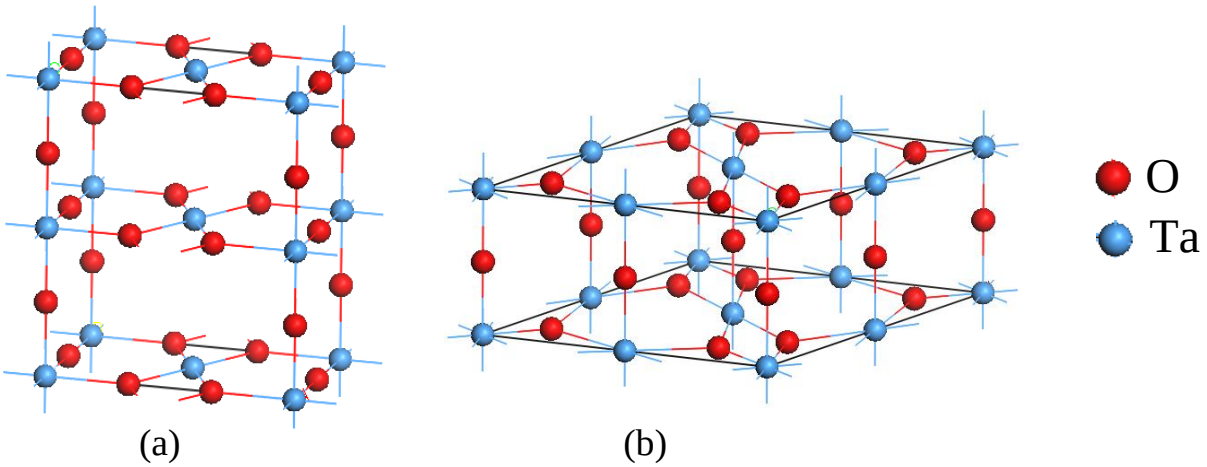

Figure 3.1: Schematic diagram of: (a) β-Ta_2O_5, (b) δ-Ta_2O_5

The band structure of Ta_2O_5 represents another controversial issue. Several research investigations have employed DFT to calculate the material band structure. Numerous functionals have been used in an attempt to get closer to the experimental results. Using Generalized Gradient Approximation (GGA), Gu *et al.*[71] arrived at a bandgap of 0.2 eV and 1.06 eV for β-Ta_2O_5 and δ-Ta_2O_5, respectively. This result was asserted by Wu *et al.* [77] who reported a similar bandgap of 0.1 eV and 1.1 eV for β- and δ-Ta_2O_5, respectively. However, the calculated bandgaps are very far from the experimentally reported bandgap [78-80], which would hinder further study on Ta_2O_5 such as studying the effect of doping on its electrical and optical properties. This underestimation is expected as the exchange-correlation functional in GGA does not contain the correct 1/R dependence (R is the charge separation distance) [81]. Hubbard correction factor (U-correction) is one of the methods used to overcome this underestimation [82]. Ivanov *et al.*[83] implemented GGA+U to calculate the bandgap of δ-Ta_2O_5, achieving 1.31 eV compared to 1.2 eV without U-correction. Unfortunately, the U-correction did not give enough improvement to the calculation and therefore other methods have been investigated. Hybrid functionals may overcome this problem through the incorporation of the exact Hartree-Fock exchange functional [81]. Wu *et al.* [77] used Heyd-Scuseria-Ernzerhof hybrid functional (HSE06) [84, 85], trying to get a more accurate result than that obtained by GGA. Their calculated bandgap was 0.9 eV and 2.0 eV for β- and δ-Ta_2O_5, respectively. This is one step closer to the practical results. However, it is not close enough to experiments.

The above introduction shows that there is a lot of controversy about the crystalline structure as well as the electronic properties of Ta_2O_5. This opens the door for further improvement and suggestion of new structures that fit better with experimental data. In the next section we calculate the band structure of β- and δ-Ta_2O_5 using hybrid functionals, which

allowed us to reduce the error in the calculated bandgao from 75%, using GGA-PBE, to 25% using PBE0 hybrid functional. We then propose a new structure for Ta_2O_5. The calculate bandgap for this structure is 3.7 eV, which is only 5% off the experimental value. This is very helpful since it allows for more quantitative analysis of the electrical and optical properties of Ta_2O_5 system and facilitates the design of an efficient photoanode for photoelectrochemical cells through incorporation of dopants which tunes the bandgap.

3.1 Bandgap Calculation of β- and δ-Ta_2O_5

Figure 3.2 (a,b) shows the energy band structures of β- and δ-Ta_2O_5 based on the GGA-PBE calculations. The β-phase has a direct bandgap of 0.2 eV whereas the δ-phase has an indirect bandgap of 1.04 eV, which occurs between the A-point and the Γ-point. The calculated bandgaps are in good agreement with calculations from previous reports [71, 77, 83].

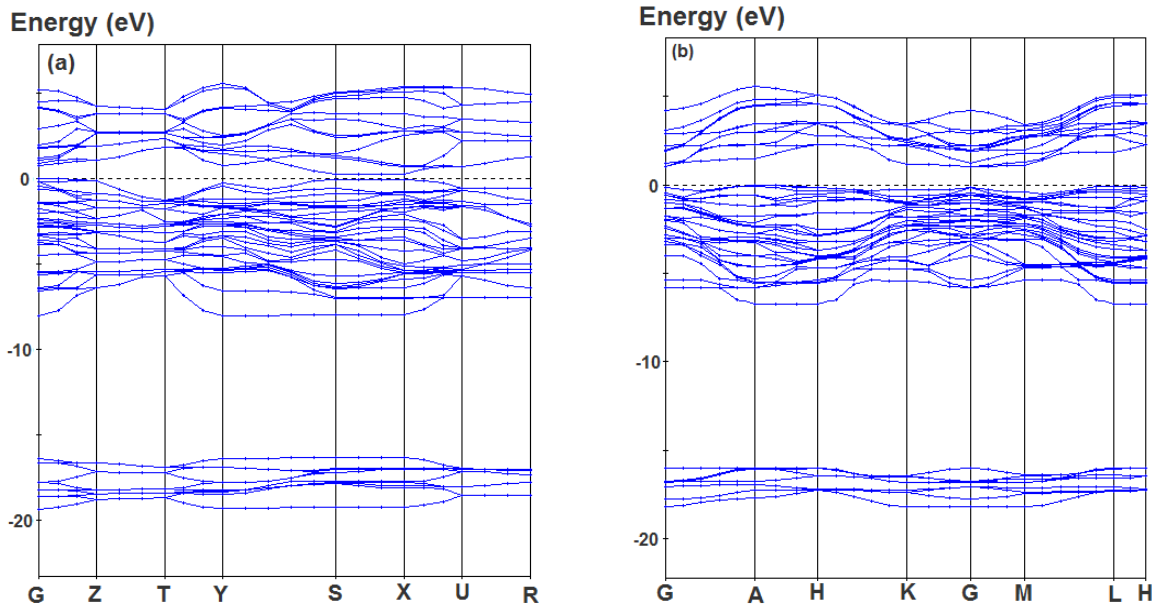

Figure 3.2: Electronic band structure of (a) β-Ta_2O_5, (b) δ-Ta_2O_5 under GGA-PBE calculation

The partial and total density of states for β- and δ-Ta_2O_5 is shown in Figure 3.3. The valence band is attributed to O 2p orbitals for both β- and δ-phases, whereas Ta 5d orbital has the main contribution to the conduction band. The partial density of states of oxygen is similar in both β- and δ-phases. On the other hand, the partial density of states of tantalum is quite different in both phases, especially in the conduction band. This is the main reason for the difference in the bandgap between the β- and δ-phases.

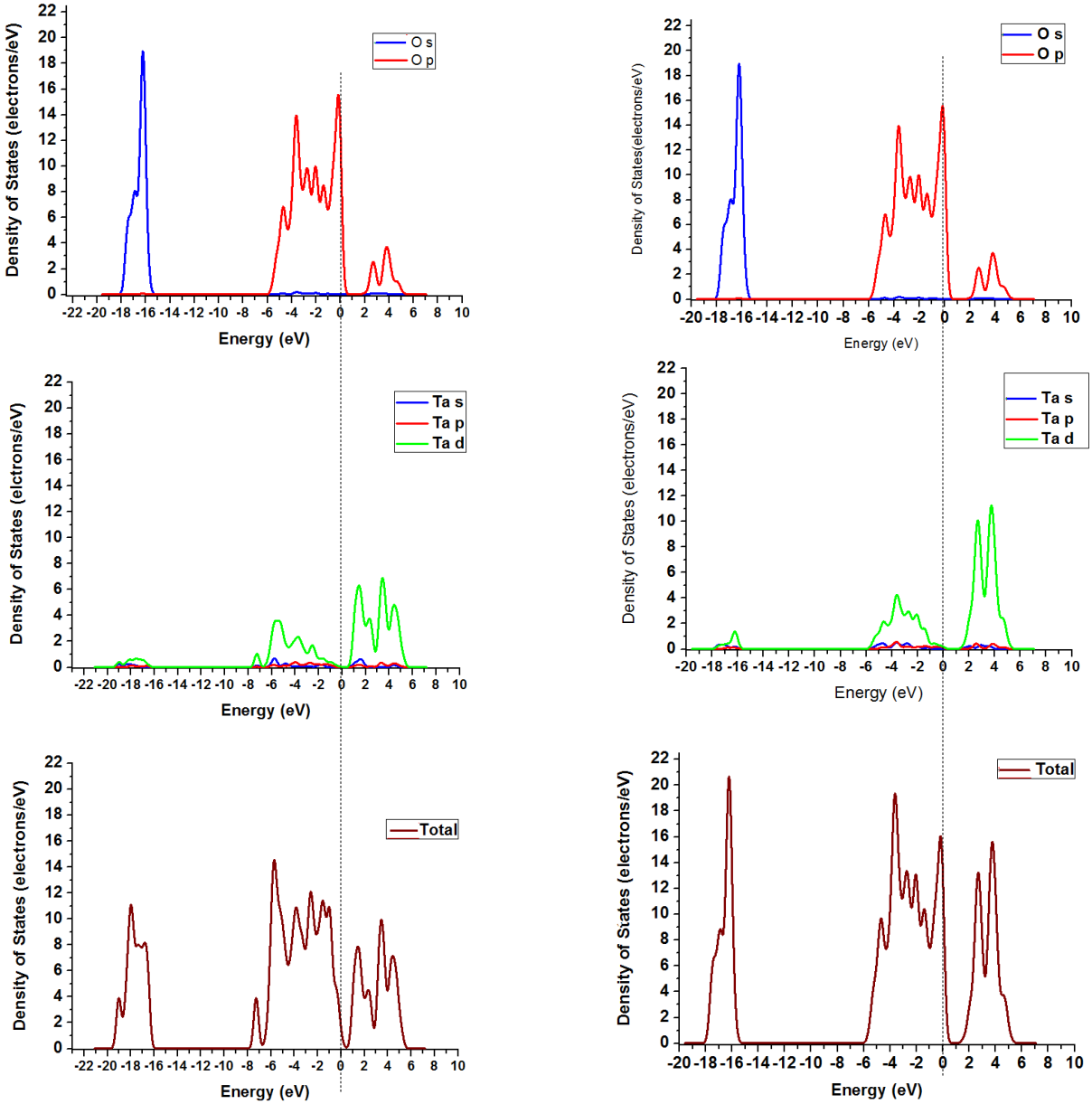

Figure 3.3: Density of states for β- (a-c) and δ- (d-f) Ta_2O_5 under GGA-PBE calculation

The results shown in Figures 3.2 and 3.3 are in very close agreement with the reported results in references [71], [77], and [83]. However, the calculated bandgap is still far from the experimental results. This is a well-known feature of pure density functional, such as PBE, that tend to underestimate the energy bandgap [80-82, 84]. Hybrid functionals are known to give more accurate results. The energy band structure for β- and δ-Ta_2O_5 based on PBE0 hybrid functional calculations are shown in Figure 3.4. The calculated bandgap for β- and δ-phases using PBE0 functional are 2.45 eV and 2.92 eV, respectively. This corresponds to a reduction in the percentage error from 73%, using GGA, to 25%, using PBE0 for δ-Ta_2O_5. In β-Ta_2O_5, the error is reduced from 95% using GGA to 37% using PBE0. B3LYP is considered another commonly used hybrid functional. We carried out bandgap calculations on β- and δ-Ta_2O_5 using B3LYP and found that it gives worse results than PBE0 for both β- and δ-Ta_2O_5. The calculated bandgap for β-Ta_2O_5 under B3LYP is 2.15 eV whereas that of δ-Ta_2O_5 is 2.65 eV. The reason why GGA gives a poorer result than hybrid functionals is due to the fact that GGA fails to correctly describe the asymptotic behavior of the exchange potential. This is remedied in hybrid funtionals through incorporating nonlocal Hartree-Fock exchange [86, 87]. It is noteworthy to mention that the two structures give comparable bandgaps under hybrid functional calculations, which suggests that Ta_2O_5 is polycrystalline with β- and δ- phases coexisting together. This is in line with the X-Ray data that shows an amorphous nature of Ta_2O_5 [88-91].

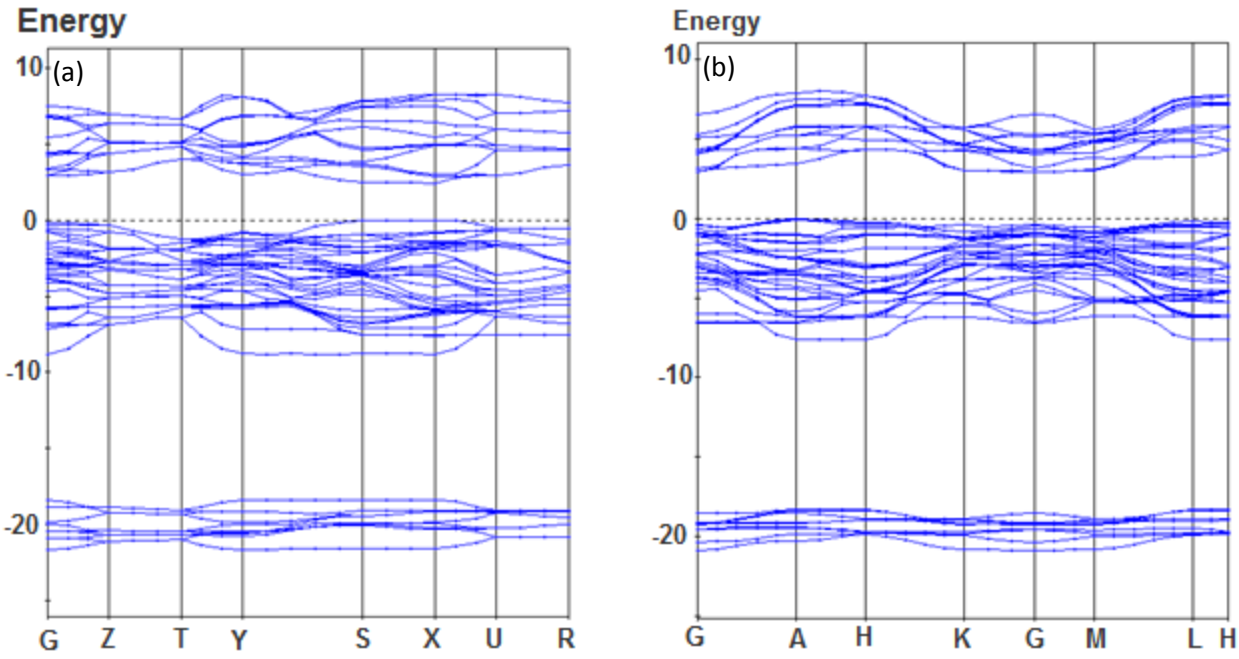

Figure 3.4: Electronic band structure for (a) β-Ta_2O_5 and (b) δ-Ta_2O_5 under PBE0 calculation

We believe that phase transformation is undertaken in Ta_2O_5 in which all the different phases are transformed to a single phase to form crystalline Ta_2O_5. This also explains the reason of having a single bandgap reported in experiments to date. If the two structures have different bandgaps as the literature suggests, there would have been two different reported experimental bandgaps. Figure 3.5 shows the partial and total density of states under PBE0 calculations for β- and δ-Ta_2O_5. By comparing Figure 3.5 with Figure 3.3 we find that both GGA-PBE and PBE0 calculations are similar with the conduction band shifted to the right in case of PBE0 to signify an increase in the bandgap. This implies that GGA-PBE is good enough for qualitative analysis whereas PBE0 can be used when quantitative results are required.

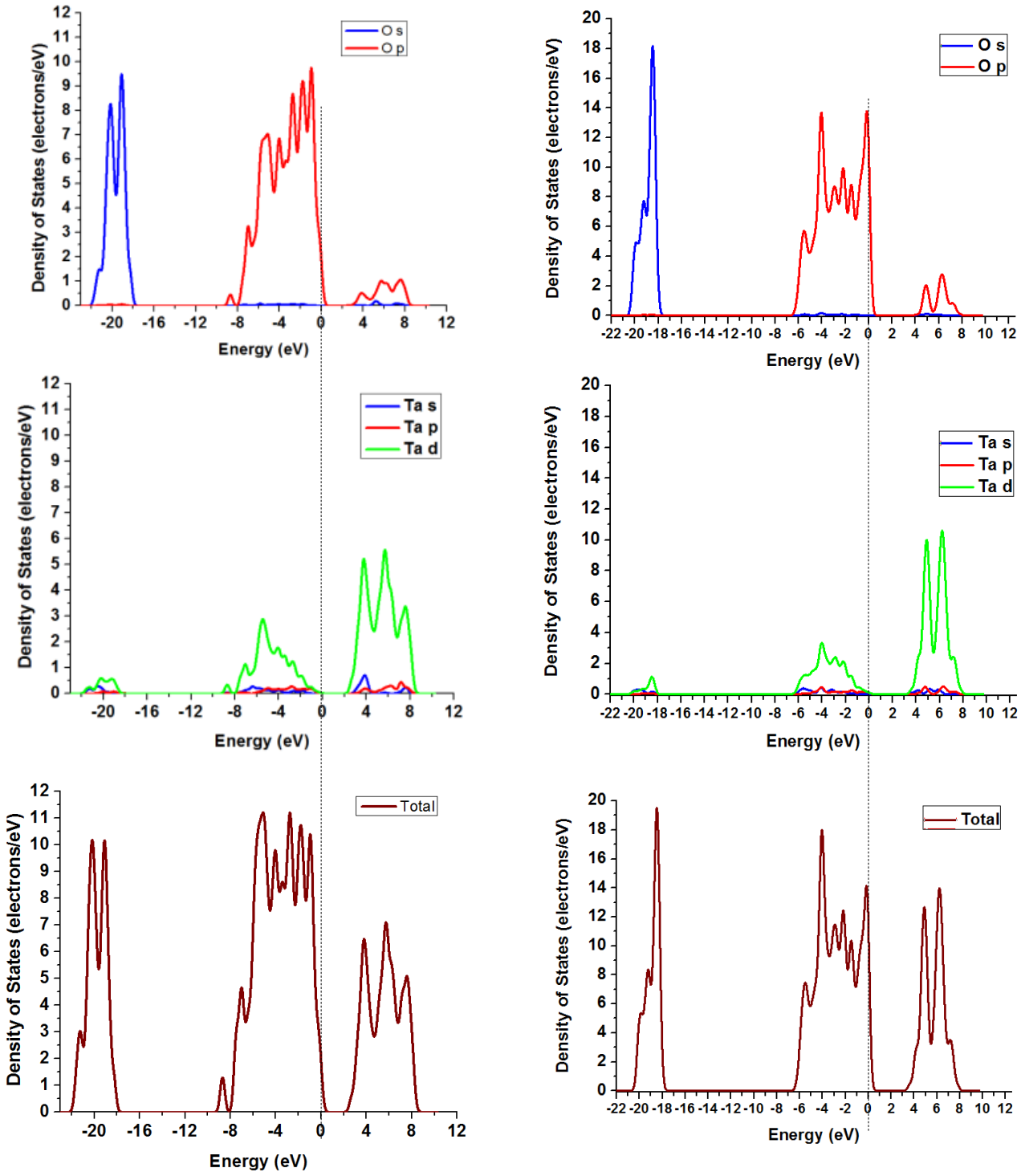

Figure 3.5: Density of states for β- (a-c) and δ- (d-f) Ta_2O_5 under PBE0 calculation

Wu *et al*. have previously used HSE06 [92, 93] hybrid functional to calculate the band gap of Ta_2O_5. However, they arrived at a bandgap of only 0.9 eV and 2 eV for β- and δ-Ta_2O_5,

respectively [77]. This corresponds to an error of 77% for β-Ta_2O_5 and 49% for δ-Ta_2O_5, compared to the measured bandgap.

The better results of PBE0 compared to HSE06 may stem from the fact that the exchange energy for HSE06 has less Hartree-Fock (HF) fraction than PBE0 as HSE06 employs HF in short range exchange only while computing the long range exchange using the pure GGA-PBE functional; however, PBE0 does not have this splitting of exchange energy terms. Knowing that the use of HF reduces the self-interaction error of density functional [94] suggests that PBE0 gives more accurate results than HSE06, in agreement with our results. To understand this in details, we need to look at the expression for the exchange-correlation expression for both functionals. For PBE0, E_{xc} is given by:

$$E_{xc}^{PBE0} = \frac{1}{4} E_x^{HF} + \frac{3}{4} E_x^{PBE} + E_c^{PBE} \tag{3.1}$$

where E_x^{HF} is the Hartee-Fock (HF) exchange energy, E_x^{PBE} is the exchange energy based on PBE functional, and E_c^{PBE} is the correlation energy which is also based on PBE functional. In HSE06, the exchange energy is split into two regions: short range and long range, with a parameter ω that determines the separation range. Only the short range part is a mixture between HF and PBE functional, whereas the long range is expressed in terms of PBE without including HF. The resulting expression for the exchange correlation energy is given by:

$$E_{xc}^{HSE} = \frac{1}{4} E_x^{HF,SR}(\omega) + \frac{3}{4} E_x^{PBE,SR}(\omega) + E_x^{PBE,LR}(\omega) + E_c^{PBE} \tag{3.2}$$

where $E_x^{HF,SR}(\omega)$ is the short range exchange energy based on HF calculations, $E_x^{PBE,SR}(\omega)$ and $E_x^{PBE,LR}(\omega)$ are the short range and long range PBE exchange energy respectively. By comparing equations (3.1) and (3.2) we can see that the correlation energy is the same for both hybrid fuctionals, however, the exchange energy for HSE06 has less HF fraction than PBE0 since HSE06 employs HF in short range exchange only while computing the long range exchange using the pure PBE functional.

An earlier version of HSE06, called HSE03 [93], has been assessed for the evaluation of bandgaps. HSE03 is similar to HSE06 with the only difference being the splitting parameter, ω. In HSE03, two different values of ω are used for HF and PBE exchange. On the other hand, for HSE06, $\omega_{HF} = \omega_{PBE}$. Krukau *et al.* [95] showed that HSE06 introduces more error than HSE03 in calculating the bandgap and that the deviation between the two functionals decreases by decreasing the value of ω used in HSE06 calculations. Therefore, it is relevant here to mention the comparison between HSE03 and PBE0 since we are sure that HSE06 would give worse, or at most equivalent, results to HSE03. Heyd *et al.* used HSE03 to calculate the bandgap of forty semiconductors and insulators [92]. The mean absolute error was calculated to be 0.26 eV. However, the method tends to greatly underestimate solids with large bandgaps. For example, the error in calculating MgO bandgap was 0.72 eV, which is about three times higher than the mean absolute error. Paier *et al.* has also compared between HSE03 and PBE0 in calculating the bandgap of MgO [96]. PBE0 showed an error of 0.46 eV compared to 1.36 eV for HSE03. This is in agreement with our results since Ta_2O_5 is considered as a relatively high bandgap material with a bandgap of about 4 eV. Another advantage of PBE0 over HSE06 is that PBE0 is

parameter-free whereas HSE06 depends on the splitting parameter (ω), whose optimum value might vary according to the system of consideration.

3.2 Proposed Structure

Our proposed structure (Figure 3.6a) involves re-orienting the conventional β-Ta_2O_5 (Figure 3.6b) such that the b-vector becomes along the Z-axis and the c-vector is in the XY plane. After that, a P1 symmetry is imposed on the structure to maximize the number of degrees of freedom for the arrangement of atoms. We then optimized the unit cell and looked for the nearest symmetry group. The cell consists of 2 Ta atoms and 5 O atoms. This is the most primitive Ta_2O_5 crystal structure. Having such primitive structure would decrease the computational time considerably, allowing for more detailed computations. Note that the original β-structure can be reconstructed from a 1×2×1 super cell of the modified β-structure. The proposed structure has an orthorhombic crystal lattice with PMMM symmetry group. The lattice parameters were optimized till we reached a = 7.9 Å, and b = c = 3.75 Å. These values are comparable with those found in ref. [70]. The calculated density is about 6.6 g/cm^3. The calculated density is in good agreement with the tabulated experimental density of amorphous Ta_2O_5, which lies in the range 5-7.2 g/cm^3 [97]. It is also in agreement with the calculated results reported by Wu *et al.* [77]which showed a density of 6.82 g/cm^3.

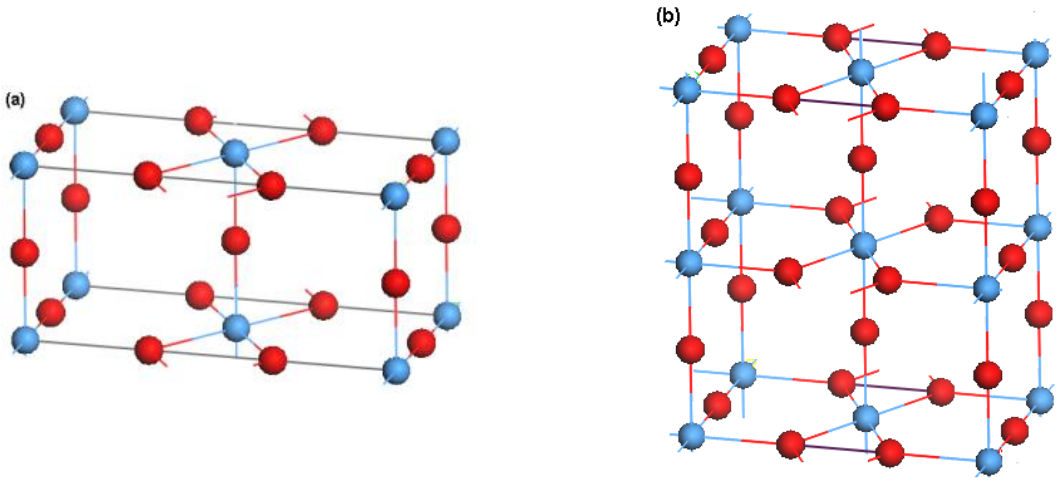

Figure 3.6: (a) Proposed Ta_2O_5 crystal structure, (b) conventional β-structure

To determine the bandgap, two levels of computation were carried out: the pure GGA-PBE functional and the hybrid PBE0 functional. The electronic structure under both levels of computations is shown in Figure 3.7. Under pure PBE functional, the calculated bandgap is 1.45 eV, which is about 0.4 eV higher than δ-Ta_2O_5 calculated under the same conditions. For PBE0 method, the calculated bandgap of the proposed structure was 3.7 eV. This is only 0.2 eV far from the reported experimental results, corresponding to a relative error of only 5%. It is worth mentioning here that the computational time for our proposed structure is six times less than β- and δ-structures. This allows for carrying out detailed computations on large supercells with relatively viable computational cost.

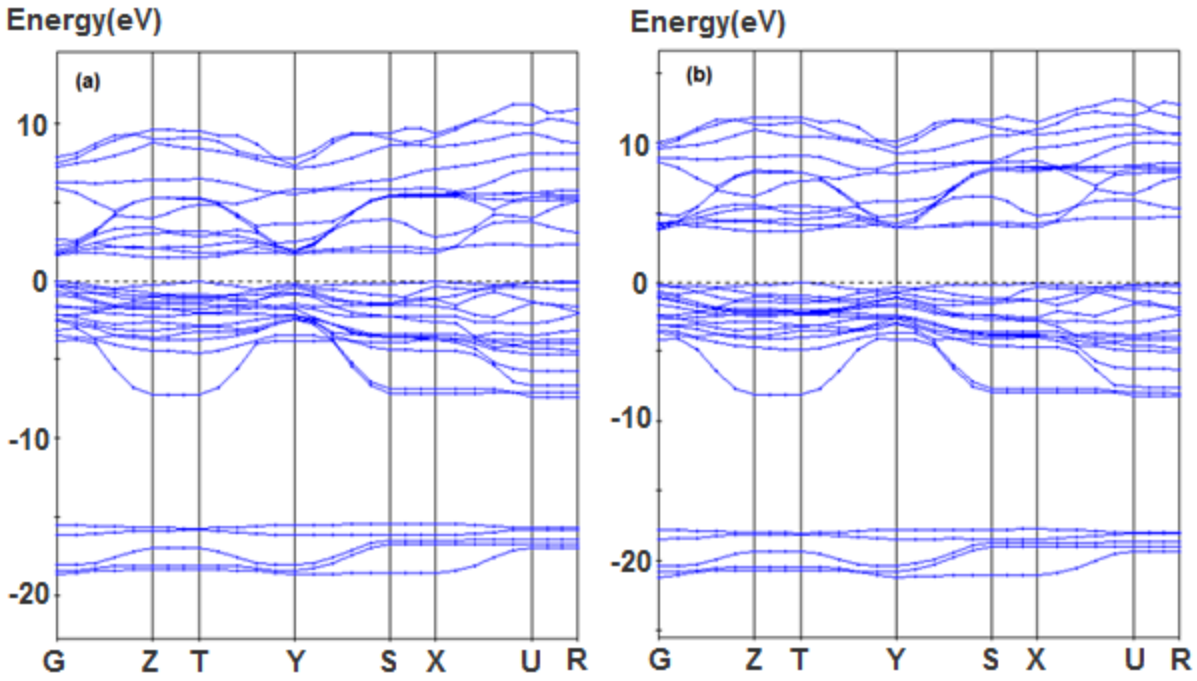

Figure 3.7: Electronic band structure of the proposed Ta_2O_5 structure under (a) GGA-PBE and (b) PBE0 calculations

For comparison purposes, Table 3.1 shows the computed bandgap for different Ta_2O_5 polymorphs using different functionals as compared to the experimental value. Note that the calculated bandgap of our proposed structure under PBE0 is the closest to experimental value. Figure 3.8 shows the partial and total density of states of our proposed structure under GGA-PBE and PBE0 calculations, respectively. As was the case with β- and δ-Ta_2O_5, O 2p forms the valence band of Ta_2O_5 whereas the conduction band is mainly formed of Ta 5d.

Table 3.1: Calculated bandgap of β-, δ-, and proposed-Ta_2O_5 using GGA-PBE, B3LYP, and PBE0 functionals

Structure	Calculated Bandgap (eV)		
	GGA-PBE	B3LYP	PBE0
β-Ta_2O_5	0.2	2.15	2.45
δ-Ta_2O_5	1.04	2.65	2.92
Proposed Structure	1.45	2.71	3.7

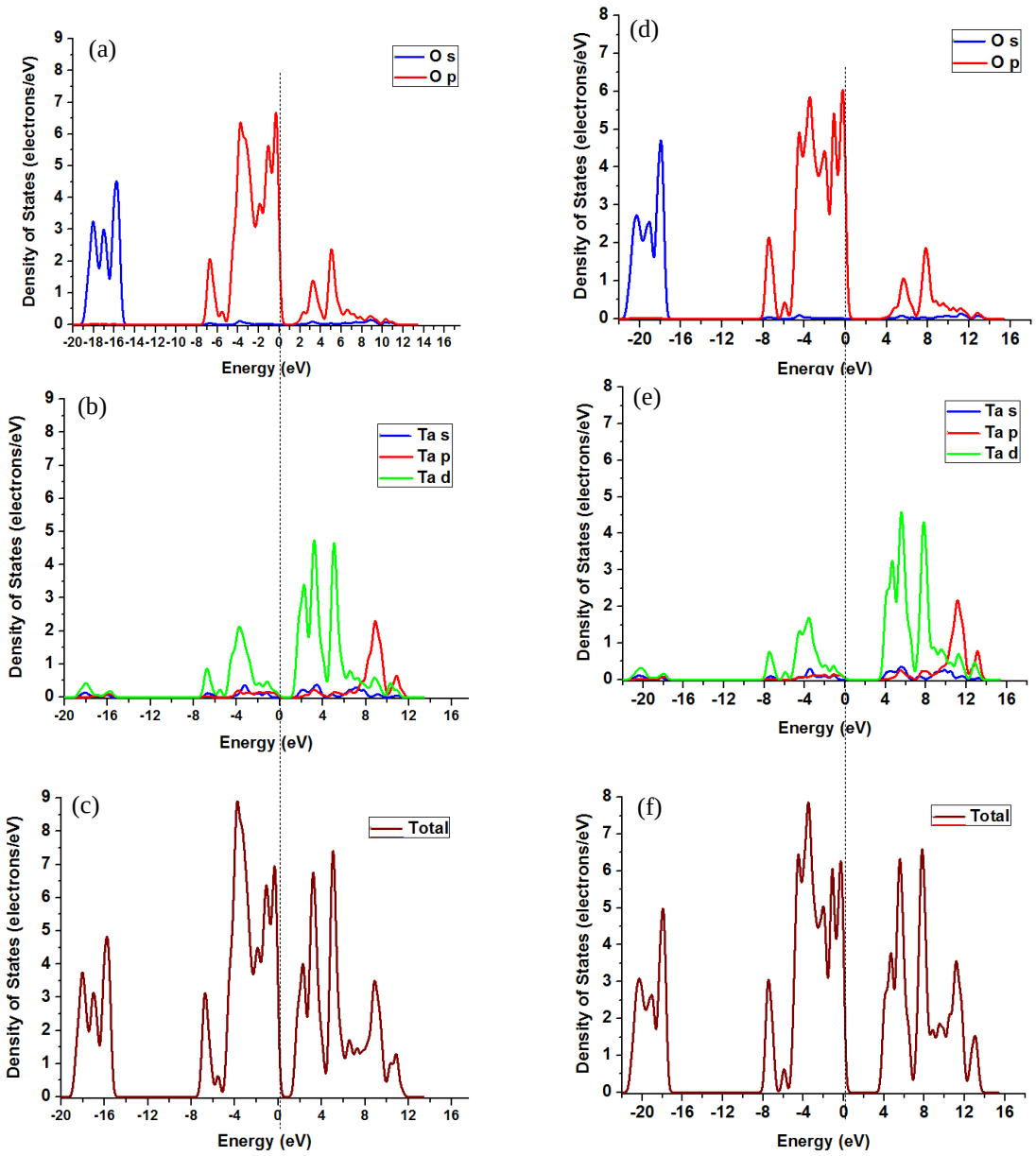

Figure 3.8: (a),(d) Partial Density of States of O atoms in proposed Ta_2O_5; (b),(e) Partial Density of States of Ta in proposed Ta_2O_5; (c),(f) Total Density of States of proposed Ta_2O_5. (a)-(c) uses GGA-PBE calculation and (d)-(f) uses PBE0 calculation

3.3 Calculated Electronic Structure of Ta-W-O System

3.3.1 Band Structure

Figure 3.9 shows the band structure of W-doped Ta_2O_5. For the sample containing 8.3% W, the effect of W appears as an impurity state near the conduction band. However, as the W content increases, the band structure is significantly modified and the conduction band edge moves downwards. This is in agreement with the findings of Wang *et al.*[98]. We find that the bandgap monotonically decreases from 3.7 eV in pristine Ta_2O_5 to 2.77, 2.07, and 1.04 eV for 8.3%, 25%, and 50% of W content, respectively. The reduction in bandgap with increasing W content can be understood from the density of states plotted in Figure 2.10. In particular, the partial density of states of Ta and O as well as the total density of states in pristine Ta_2O_5 are illustrated in Figure 3.10. The valence band maximum (VBM) is dominated by O 2p orbitals whereas the conduction band minimum (CBM) is dominated by Ta 5d orbitals, in agreement with Refs [60, 99, 100]. Therefore, substituting Ta with W is expected to modify the conduction band while keeping the valence band intact. Figure 3.10c shows that the total density of states of the doped Ta_2O_5 near the CBM agrees very well with the partial density of states of W 5d shown in Figure 2.10d. This asserts that the reduction in the bandgap is due to the incorporation of W. The CBM is shifted downwards because W 5d orbital has lower energy than Ta 5d orbital[101]. Note that the energy of the VBM remains nearly constant for all doped structures. However, its k-position seems to shift towards point B as the concentration of W increases. In fact, a closer look at the band structure shows that as the concentration of W increases, the shift of the VBM towards B point is accompanied by a lowering of the conduction band states at points B and X. This also suggests another transition between the VBM and the conduction band state at point B, which has a larger energy gap but lower momentum change and hence high probability of transition.

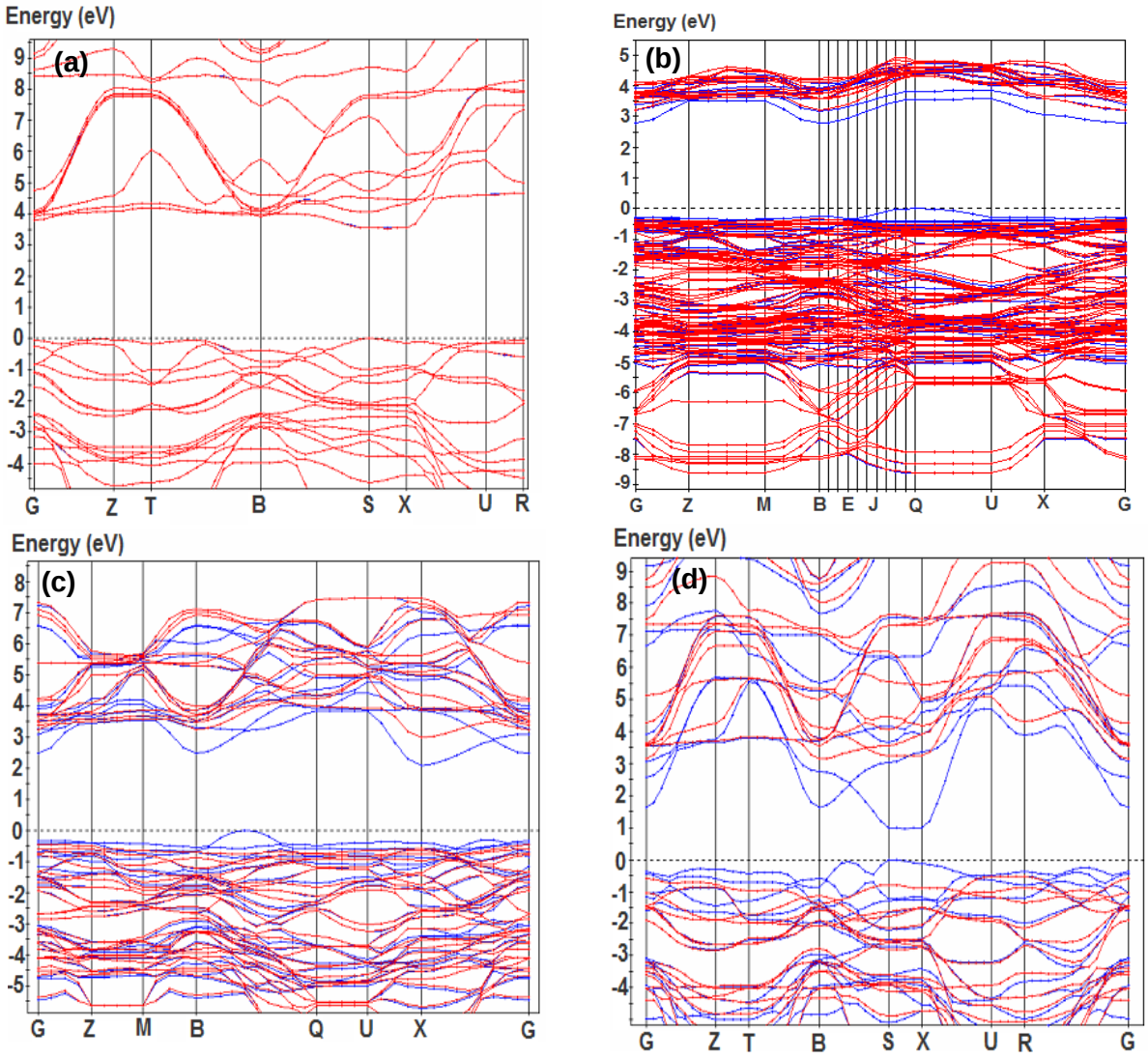

Figure 3.9: Band structure for (a) pristine Ta_2O_5, (b) 8.3%W, (c) 25%W, and (d) 50%W-doped Ta_2O_5 under PBE0 calculation

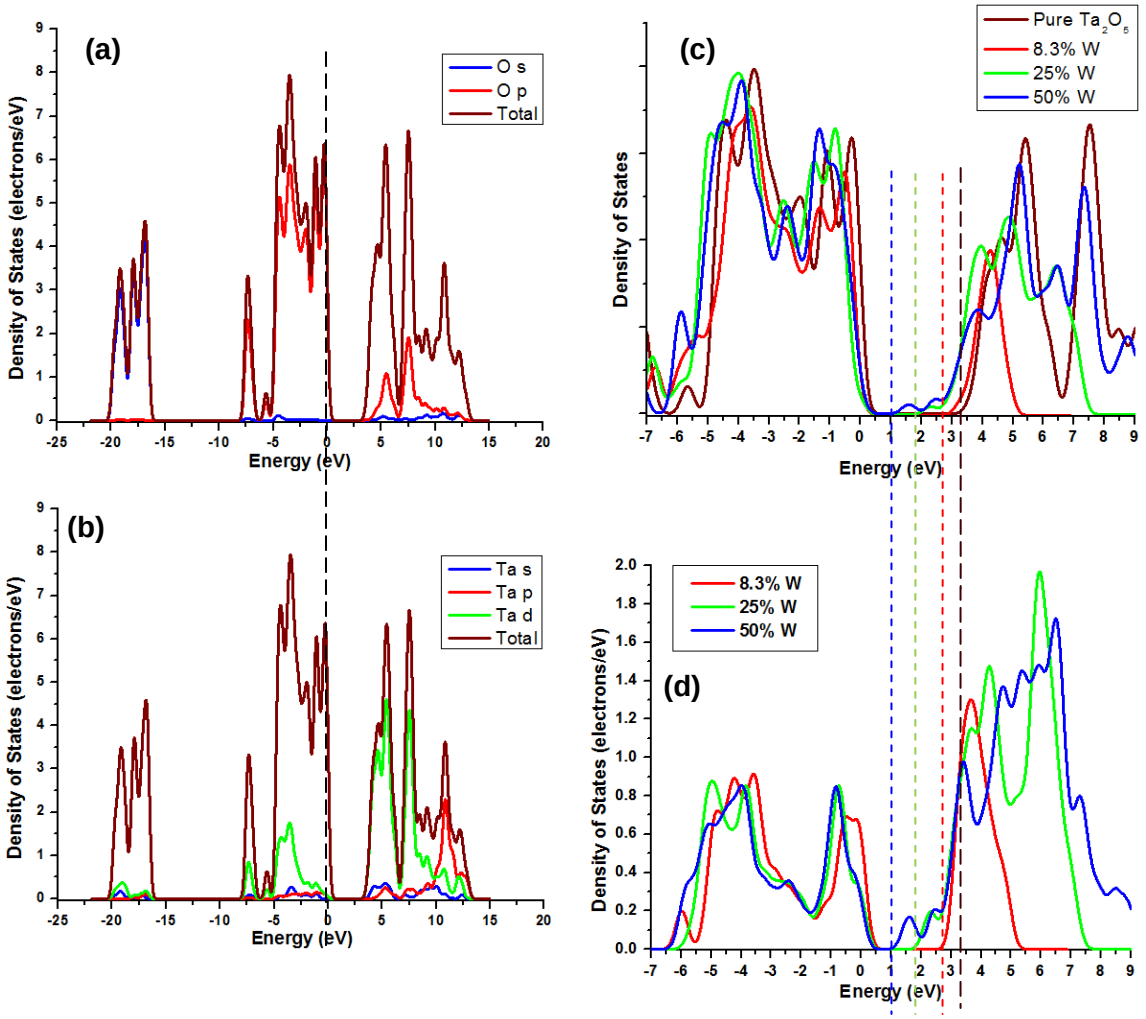

Figure 3.10: (a,b) Partial and Total Density of States in pristine Ta_2O_5, (c) Total Density of States in pristine as well as Ta-W-O alloys, (d) Partial Density of States due to W 5d for different Ta-W-O alloys

Note also the change in the VBM and CBM positions upon the incorporation of W, resulting in the formation of indirect bandgaps. The material becomes highly indirect upon the addition of a small amount of W, with the phonon momentum, required for the electron excitation, increasing by more than three times at 2.5% W compared to pristine Ta_2O_5. However, as the amount of W increases, the material becomes less indirect, going back to its initial state at 50% W. Table 1 and Figure 3.11 summarize the effect of W content on the band structure of Ta_2O_5. It can be seen that both the bandgap and the phonon momentum decrease with increasing the W content, two effects in the right direction. It is worth mentioning that although the electronic transition between VBM

and CBM is highly indirect at 25% W content, there exists another possible transition between VBM and point B in the conduction band. This transition is more direct and hence have larger absorption coefficient, requiring a phonon momentum of 3.95×10^{-25} N.s, which is about half that required for the transition between VBM and CBM, with a photon energy of around 2.4 eV, which is still very close to the optimum value.

Table 3.2: Valence Band Maximum, Conduction Band Minimum and the corresponding required phonon momentum for electron excitation at different W content

Structure	k-value of VBM	K-value of CBM	Phonon Momentum $\times10^{-25}$ (N.s)
Pristine Ta_2O_5	(-0.5, 0.5, 0)	(-0.25, 0.5,0)	2.1
8.3%W	(0.5,0.5,0.5)	(0, 0, 0)	6.8
25%W	(0.5,0.2,0.2)	(0, 0.5, 0)	7.0
50%W	(-0.5, 0.5, 0)	(-0.25, 0.5,0)	2.1

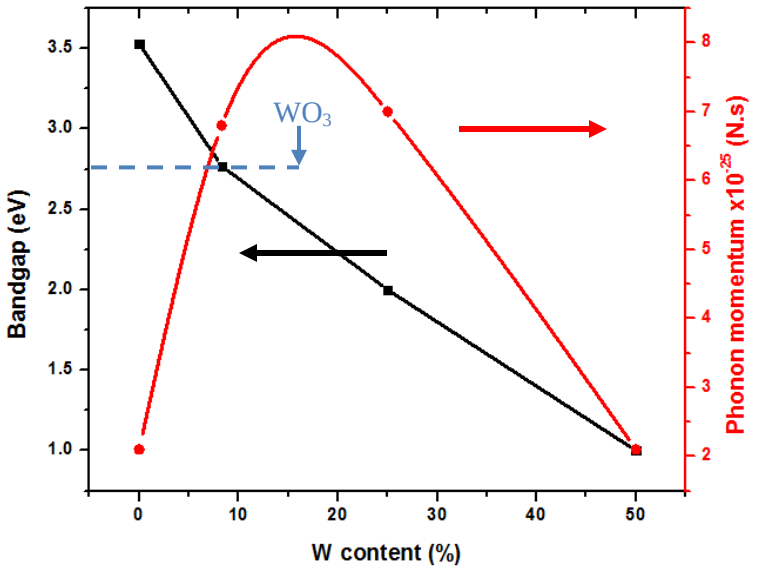

Figure 3.11: The bandgap (red) and phonon momentum (black) required for electron transition in Ta-W-O as a function of W concentration

In conventional mixed metal oxide systems, the bandgap decreases till it reaches the value of the constituent metal oxide with the lower bandgap. For example, upon increasing the content of Fe in the Ti-Fe-O system, the bandgap of the mixed metal oxide initially decreases from 3.2 eV (the

bandgap of TiO_2) to 2.1 eV (the bandgap of Fe_2O_3)[102]. Afterwards, the bandgap remains constant irrespective of the amount of Fe added[102]. However, Figure 3.11 shows a very interesting phenomenon. At W content greater than 17%, the bandgap of the Ta-W-O system falls below 2.4 eV, the bandgap of pristine WO_3. In other words, the bandgap of the mixed metal oxide becomes lower than the bandgaps of its constituent metal oxides (Ta_2O_5 and WO_3). This phenomenon can be understood from the expression for the bandgap of any semiconductor alloy, A_xB_{1-x}, where A and B are the pristine semiconductors forming the alloy. In most semiconductor alloys, the alloy bandgap can be determined as the weighted average of its semiconductor constituents[103]:

$$E_g^{AB}(x) = xE_g^A + (1-x)E_g^B \tag{3.1},$$

where x denotes composition, E_g^{AB} is the bandgap of the alloy, E_g^A and E_g^B are the bandgaps of constituent A and B, respectively. Equation (3.1) guarantees that the bandgap of the alloy always lies between that of its constituents. However, some semiconductor alloys deviate from such linear relationship to have a quadratic form[104]:

$$\Delta E_g^{AB}(x) = bx(x-1) \tag{3.2},$$

where b is known as the *bowing parameter* and is generally composition independent. It is thought that the bowing parameter is originated from three distinct physical contributions: (i) volume change due to the change in the lattice constants of the alloy constituents when they form the alloy; (ii) charge exchange occurring when a highly electronegative atom substitutes a less electronegative atom, which creates localized energy levels close to the CBM that interacts with

the extended states and lowers the conduction band; (iii) structural relaxation due to the relaxation of the cation-anion bond lengths in the alloy[103, 104].

Using equations (3.1) and (3.2) and the data given in Figure 3.11, the calculated bowing parameter for Ta-W-O system shows a very large and composition dependent bowing parameter of -8.6, -6.1, and -7.7 for the materials containing 8.3% W, 25% W, and 50% W, respectively. A similar phenomenon was reported for GaAsN alloys[104]. While for GaAsN system the bowing parameter monotonically decreased with increasing N concentration, for Ta-W-O system, the bowing parameter shows a minimum value at ~25% of W content. In the GaAsN system, the large bowing parameter was due to the localized energy state that N introduces below the conduction band of GaAs[104]. This localized state has a strong charge exchange with the conduction band and it essentially brings the conduction band edge downwards leading to a decrease in the bandgap. In such system the bowing parameter decreases with increasing the N content because the N 2p orbital is merged with the extended states in the conduction band at higher N concentration and thus it is no longer localized. Therefore, the charge exchange effect is no longer valid. This suggests that for Ta-W-O system, there would be different mechanisms causing the bowing parameter at different W concentrations. We think that at 8.3%W, the dominant contribution to the bowing parameter is charge exchange, similar to GaAsN system. This is asserted by Figure 1b, which shows a localized W 5d state close to the extended states that strengthens charge exchange. Note also that the band structure for 8.3%W is significantly different from pristine Ta_2O_5 (compare Figures 3.9a and b) where the bandgap becomes considerably indirect indicating a strong interaction between W and Ta_2O_5 orbitals. At 25% of W content, the bowing parameter is still high but it is less than the 8.3% W case, indicating that the contribution of charge exchange is reduced, which is confirmed by the decreased indirect

bandgap that moved closer to that of pristine Ta_2O_5. For 50% of W content, the indirect bandgap is exactly the same as pristine Ta_2O_5, which infers a minimum interaction between W and Ta_2O_5 orbitals. However, the bowing parameter for 50% is higher than its 25% W counterpart, indicating that another mechanism is contributing to the bowing parameter. At this high concentration, the W atoms tend to cause volume change in the crystal lattice due to the different ionic radii of Ta_2O_5 and WO_3.

3.3.2 Hole Effective mass

Although the band structure calculations using GGA-PBE functional underestimate the bandgap of systems with strongly correlated electrons, they can still give a qualitative estimation of the effective mass because the effective mass depends on the curvature of the VBM and CBM rather than on their values. Figure 3.12 shows the band structures using GGA-PBE functional in which the valence band maximum is designated by a circle, asserting the fact that VBM and CBM still preserve their curvature under GGA calculations. In this study, we focus on the effective mass of holes only because the water splitting device is a minority carrier device and the Ta-W-O system is an n-type semiconductor. Note that a low effective mass is a desirable property providing a high charge carrier mobility and correspondingly, a high solar-to-hydrogen conversion efficiency[101].

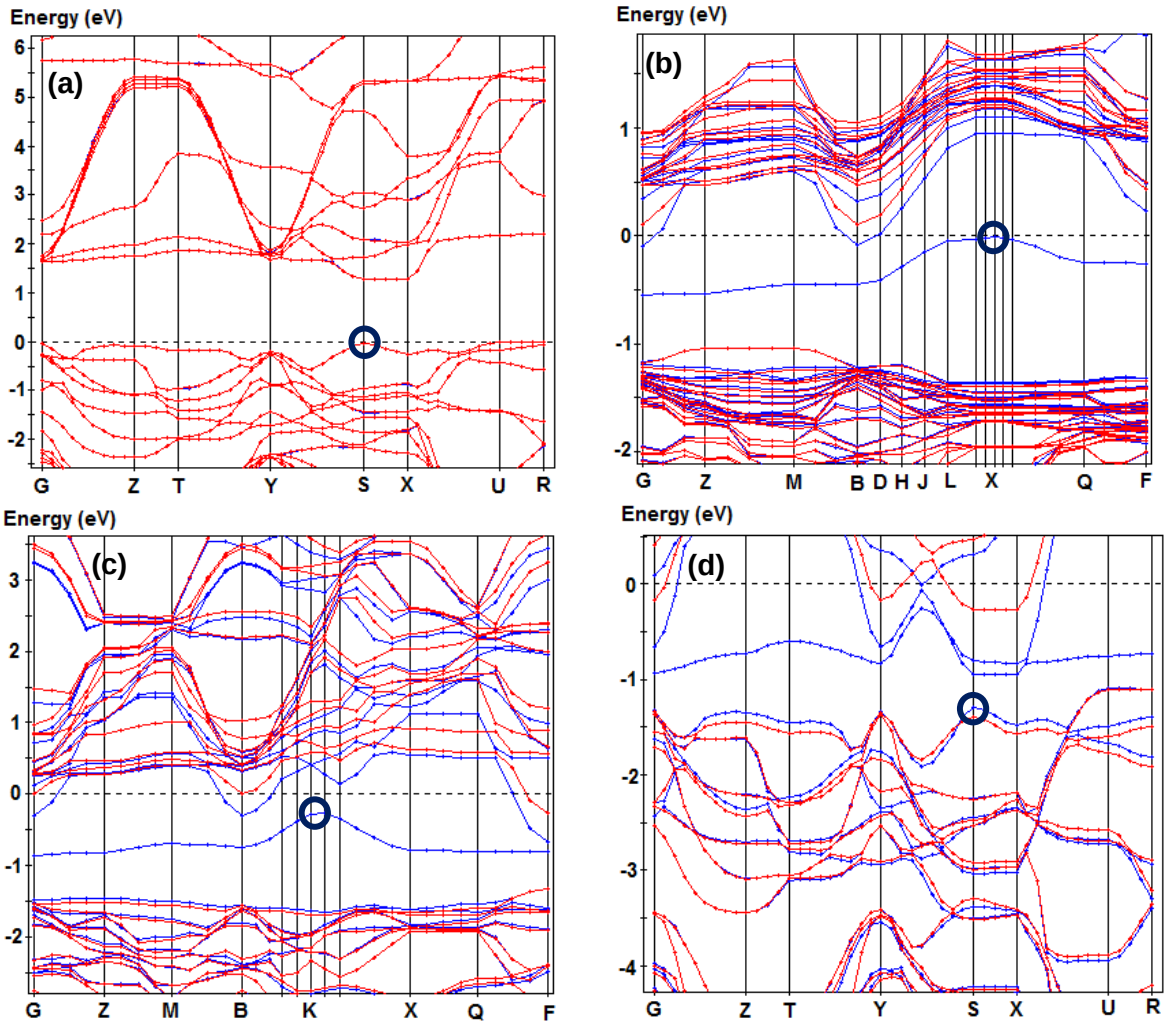

Figure 3.12: Band structure of (a) pristine Ta_2O_5, Ta_2O_5 containing (b) 8.3%W, (c) 25%W, and (d) 50%W under GGA-PBE Calculation. Note the circle which signifies the valence band minimum as compared to Figure 3.9

The effective mass tensor is given by [105]:

$$\frac{1}{m} = \begin{pmatrix} \frac{\partial^2 \varepsilon}{\partial k_x^2} & \frac{\partial^2 \varepsilon}{\partial k_x \partial k_y} & \frac{\partial^2 \varepsilon}{\partial k_x \partial k_z} \\ \frac{\partial^2 \varepsilon}{\partial k_y \partial k_x} & \frac{\partial^2 \varepsilon}{\partial k_y^2} & \frac{\partial^2 \varepsilon}{\partial k_y \partial k_z} \\ \frac{\partial^2 \varepsilon}{\partial k_z \partial k_x} & \frac{\partial^2 \varepsilon}{\partial k_z \partial k_y} & \frac{\partial^2 \varepsilon}{\partial k_z^2} \end{pmatrix} \tag{3.3}$$

where ε is the energy at the specified k-point. To calculate the second derivatives given in equation (3.3), finite difference approximation was implemented by

$$\frac{\partial^2 \varepsilon}{\partial k_i^2} = \frac{1}{(\Delta k_i)^2}\left[\varepsilon(k_i + \Delta k_i, k_j, k_k) - 2\varepsilon(k_i, k_j, k_k) + \varepsilon(k_i - \Delta k_i, k_j, k_k)\right] \tag{3.4}$$

and

$$\frac{\partial^2 \varepsilon}{\partial k_i \partial k_j} = \frac{1}{(2\Delta k_i)(2\Delta k_j)}\begin{bmatrix} \varepsilon(k_i + \Delta k_i, k_j + \Delta k_j, k_k) - \varepsilon(k_i + \Delta k_i, k_j - \Delta k_j, k_k) \\ -\varepsilon(k_i - \Delta k_i, k_j + \Delta k_j, k_k) + \varepsilon(k_i - \Delta k_i, k_j - \Delta k_j, k_k) \end{bmatrix} \tag{3.5}$$

where $\{i, j, k = x, y, z\}$ and $\Delta k_i = \Delta k_j = \Delta k_k = 0.1$ (a.u.$^{-1}$). After computing the tensor elements, the matrix is diagonalized to find the eigenvalues and eigenvectors that is the magnitudes and the principal directions of the effective mass.

After calculating the eigenvalues, the effective mass can be calculated as follows:

$$m_{i,j,k} = \hbar^2 \left(\frac{\partial^2 \varepsilon}{\partial k_{i,j,k}^2} \right)^{-1} \tag{3.6}$$

Table 3.3 summarizes the calculated effective mass for Ta-W-O system under PBE0 and GGA-PBE functionals. Although the numbers for PBE0 and GGA-PBE are in some cases different, it should be stressed that they show the same trend. The principal axes for the effective mass were found to be x, y, and z-directions. The effective mass shows an anisotropic direction dependency by showing the smallest value in y-direction which is the most favorable direction for the hole transport. As the W content increases, the effective mass in the y-direction becomes smaller compared to other directions, making the hole transport in the y-direction more favorable. The monotonic decrease of the effective mass as a function of the W content can be attributed to the delocalization of the electron energy levels from W. At 25% and 50% of W contents, the effective mass in the y-direction is approximately $0.5m_e$ and $0.25m_e$, respectively, where m_e is the electron rest mass. It is noteworthy to mention that the effective mass of holes in TiO_2 is $(0.8\pm0.2)\ m_e$ [106], therefore Ta-W-O system is expected to have higher mobility and hence higher solar-to-hydrogen conversion efficiency. Furthermore, the effective mass of hole in Ta-

W-O system is comparable to that in III-V semiconductors, and Ta_2O_5 has a much higher dielectric constant ensuring a higher diffusion length according to the following relation:

$$L_D = \left(\frac{2\varepsilon\varepsilon_0 kT}{qN_D} \right)^{1/2} \tag{3.7}$$

where L_D is the diffusion length, ε is the relative dielectric constant, ε_0 is the permittivity of free space, k is Boltzmann constant, T is the absolute temperate, q is the electron charge, and N_D is the doping concentration. A larger diffusion length indicates less recombination of charge carrier, resulting in higher overall conversion efficiency. This suggests that Ta-W-O semiconductor alloys can replace expensive III-V semiconductors for high efficiency solar cells in space applications.

Table 3.3: Calculated effective mass for Ta-W-O using PBE0 and GGA-PBE functionals

W%	PBE0 Calculation			GGA-PBE Calculation		
	m_x/m_e	m_y/m_e	m_z/m_e	m_x/m_e	m_y/m_e	m_z/m_e
Pristine Ta_2O_5	1.52	1.09	1.27	1.55	0.89	1.55
8.3% W	1.44	0.68	20.4	1.61	0.74	21.5
25% W	2.49	0.46	14.67	2.12	0.69	15.78
50% W	3.32	0.25	0.92	1.36	0.67	1.47

CHAPTER 4

EXPERIMENTAL RESULTS

4.1 Anodization of Ta and Ta-W films

The anodization of Ta foil to form Ta_2O_5 nanotubes can be done in an electrolyte containing a mixture of concentrated HF and H_2SO_4[91, 107, 108]. However, the anodization parameters should be carefully adjusted in order to obtain nanotubes that are well-adhered to the substrate. For example, increasing the anodization time and/or HF content beyond a certain limit leads to the detachment of the nanotubes from the substrate due to the formation of TaF_5 layer between the Ta_2O_5 layer and the Ta substrate[91, 107].

Figure 4.1 shows the effect of anodization time, applied voltage, and HF concentration on the nanotube length, diameter, and wall thickness. In general, longer nanotubes can be achieved in 10%W alloy compared to 2.5%W alloy. This enhances the absorption for the 10%W alloy since it allows for a longer path for photons and hence a higher probability of photon absorption. Also the nanotube thickness for 10%W alloy is smaller than that its 2.5%W counterpart, which improves charge separation characteristics since the photo-generated charge carriers would have to move a shorter distance and hence the probability of charge recombination decreases. Furthermore, the nanotube diameter for the 2.5%W is smaller than that of 10%W. It can be seen from Figure 4.1(a,b) that anodization time has more pronounced effect on the 10%W alloy compared to that of 2.5%W. For example, the nanotube length changes from 0.84 µm to 1.2 µm for 2.5% W alloy whereas it changes from 1.2 µm to 6.4 µm for 10%W alloy as the anodization time increases from 15 minutes to 35 minutes. Increasing the anodization potential increases the nanotube length and diameter for both 2.5%W and 10%W alloys, with a higher effect on the 10%W alloy (Figure 4.1(c,d)). The nanotube thickness increases from 9 nm to 20.5 nm for the 2.5%W alloy whereas it nearly remains constant at around 10.5 nm for the 10%W alloy as the anodization potential increases from 10 V to 20 V. Although the nanotube length for the 2.5%W

alloy doesn't seem to be affected by the anodization time and the applied potential, it seems that it is influenced by the HF concentration where the nanotube length increases from 0.6 µm to 3.2 µm as the HF concentration increases from 0.51 M to 0.85 M then it decreases to 1.2 µm at 1.17 M HF (Figure 4.1e). The nanotube length, diameter, and thickness show the same dependence on HF concentration. Figure 4.2 shows selected SEM images for the nanotubes that were anodized at different conditions.

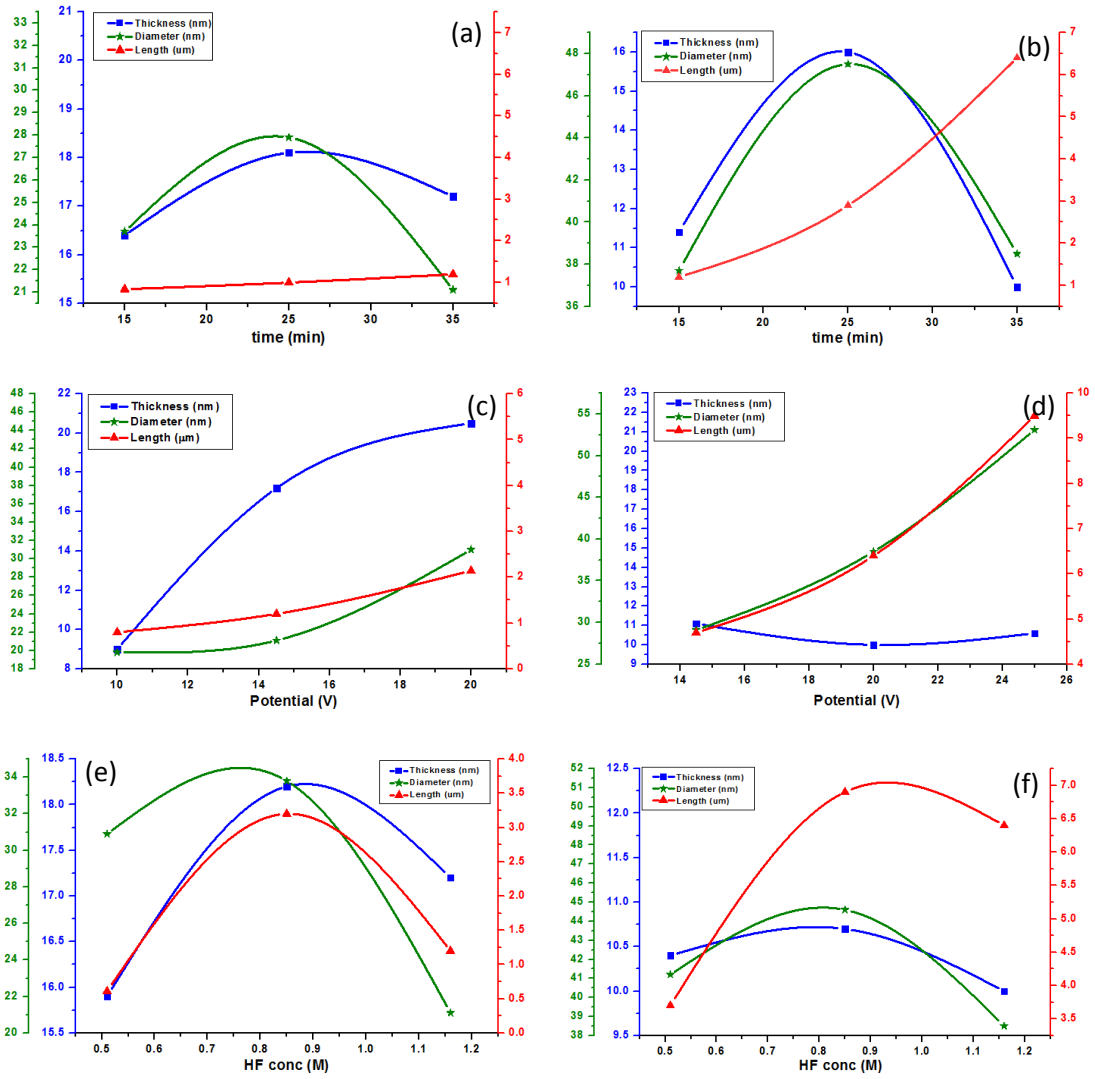

Figure 4.1: (a,b) The effect of anodization time on the nanotube length, thickness, and wall thickness for (a) 2.5%W alloy, (b) 10%W alloy. (c,d) The effect of anodization potential on the nanotube length, thickness, and wall thickness for (c) 2.5%W alloy, (d) 10%W alloy. (e,f) The effect of HF conc on the nanotube length, thickness, and wall thickness for (e) 2.5%W alloy, (f) 10%W alloy

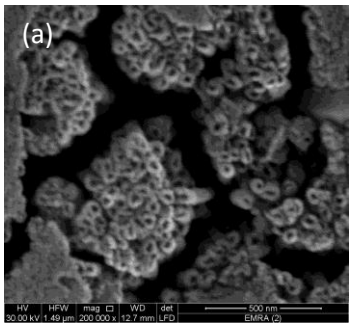

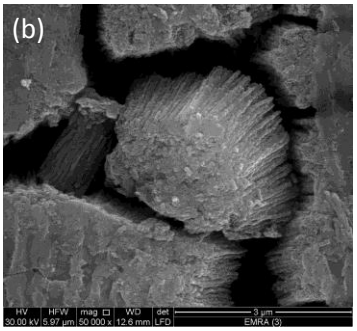

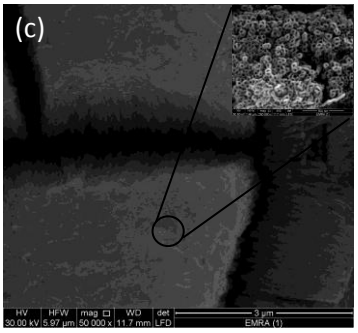

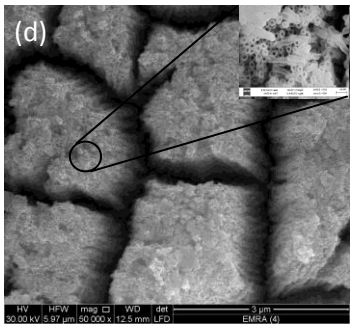

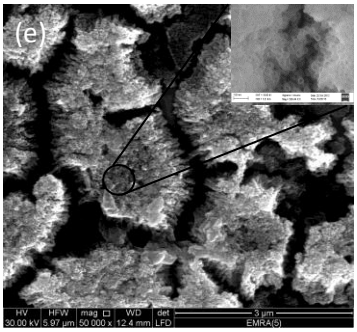

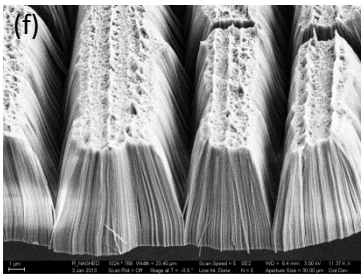

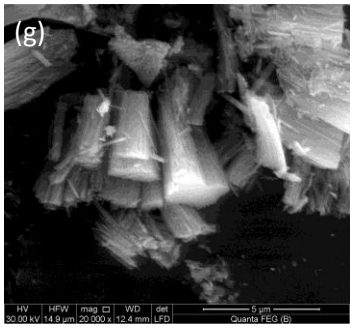

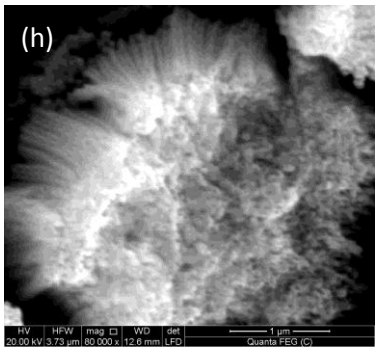

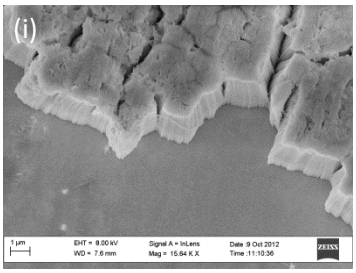

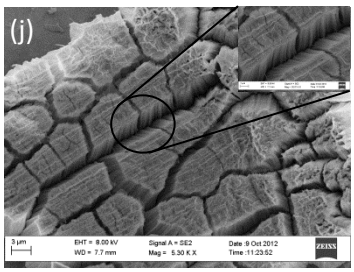

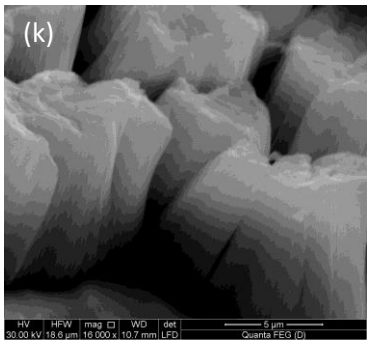

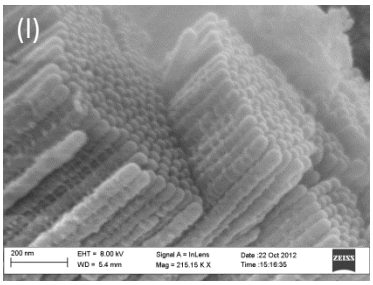

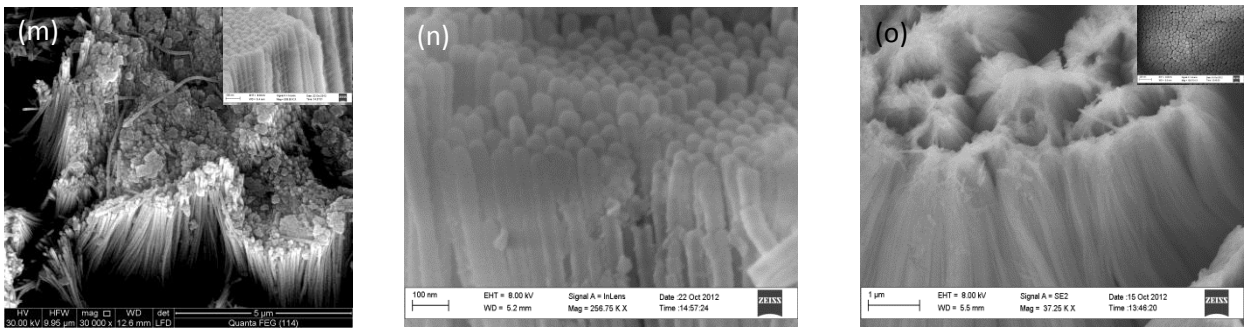

Figure 4.2: SEM images for 2.5%W alloy (a-h) and 10%W alloy (i-o). The anodization conditions are: (a) t=5min, V=14.5V, HF=1.17M, (b) t=15min, V=14.5V, HF=1.17M, (c) t=25min, V=14.5V, HF=1.17M, (d) t=35min, V=14.5V, HF=1.17M, (e) t=35min, V=10V, HF=1.17M, (f) t=35min, V=20V, HF=1.17M, (g) t=35min, V=20V, HF=0.85M, (h) t=35min, V=20V, HF=0.51M, (i) t=15min, V=20V, HF=1.17M, (j) t=25min, V=20V, HF=1.17M, (k) t=35min, V=20V, HF=1.17M, (l) t=35min, V=14.5V, HF=1.17M, (m) t=35min, V=25V, HF=1.17M, (n) t=35min, V=20V, HF=0.85M, (o) t=35min, V=20V, HF=0.51M

Although we were able to fabricate nanotubes with controlled length, diameter, and wall thickness, they don't adhere well to the substrate. This is not suitable for photoelectrochemical applications since we need to put the elecrode in a basic medium which makes the nanotubes to peel off the substrate. We found out that anodizing Ta and Ta-W foils in an electrolyte of 2.9M HF and 16.4M H_2SO_4 at 15 V lead to the formation of well-adhered nanotube oxide layer on top of the metal substrate. For the pure Ta substrate, the surface starts to crack after 4 minutes of anodization whereas it cracks after 3 and 2.5 minutes for the 2.5%W and 10%W respectively. The decrease in the maximum anodization time with increasing W content can be attributed to the stresses in the crystal lattice due to the substitution of some Ta atoms with W which caused the cracks to appear at earlier time. It is noteworthy that for pure Ta_2O_5 and 2.5%W alloy, we were able to form nanotubes after 20 seconds only whereas we had to go beyond 2 minutes of anodization for the 10%W alloy in order to obtain nanotubular structure. This is probably due to the presence of WO_3 which has different reactivity with the F^- ions than that of Ta_2O_5. This is asserted from the fact that the maximum nanotube length that we were able to obtain decreases progressively by increasing W content from 3.3 µm for pure Ta_2O_5, to 2.1 µm for 2.5%W, to 1.4 µm for 10%W. Figure 4.3 shows the SEM images for the samples anodized at 2.9M HF.

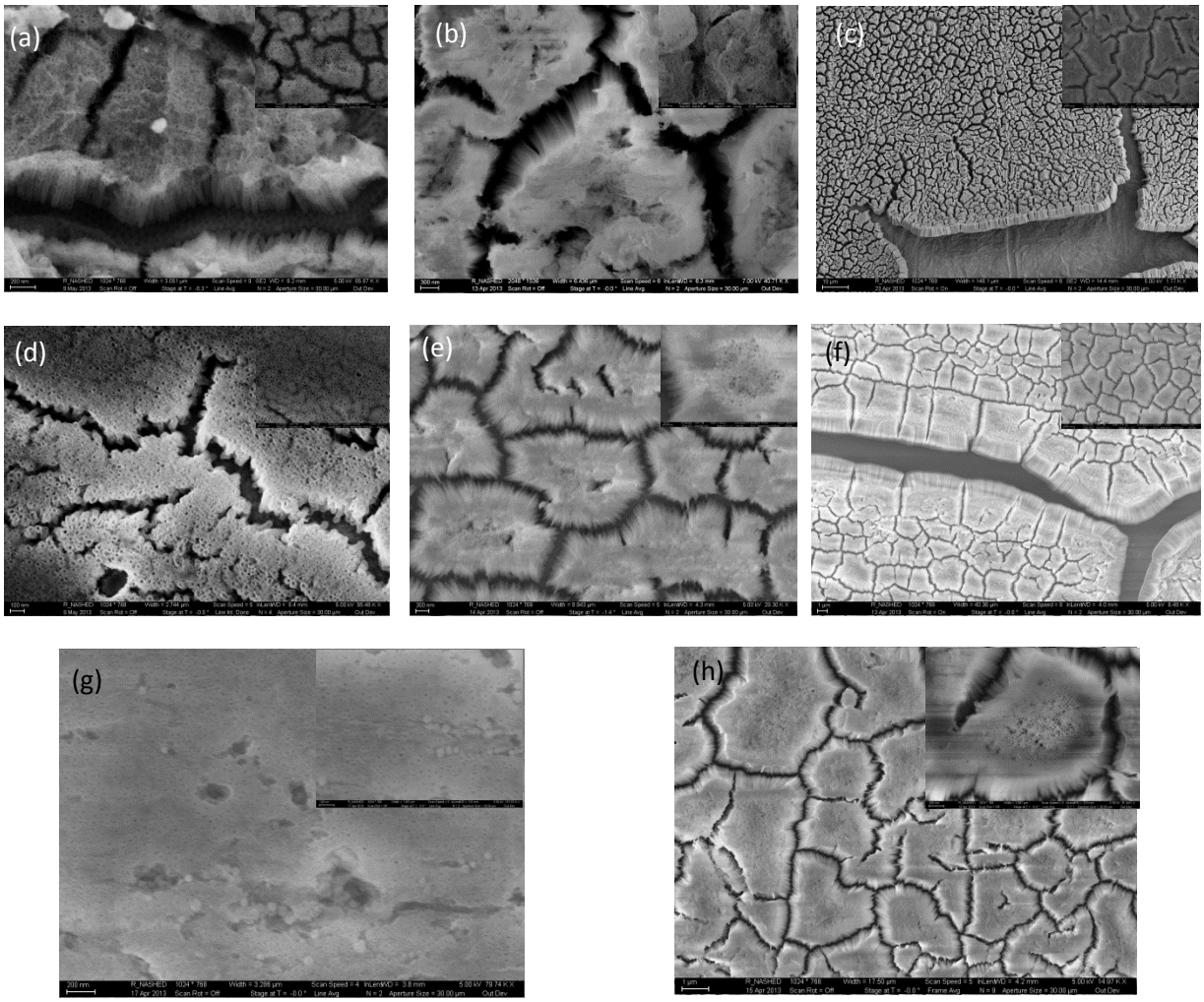

Figure 4.3: SEM images for pure Ta2O5 (a-c), 2.5%W alloy (d-f) and 10%W alloy (g,h) anodized at 15 V, 16.4M H2SO4 and 2.9M HF for (a,d) 20 seconds, (b,f) 3 minutes, (c) 4 minutes, (e,h) 2.5 minutes, (g) 2 minutes

4.2 X-Ray Diffraction

Figure 4.4 shows the XRD pattern for pristine and W-doped Ta_2O_5. It turned out that the nanotubes have an orthorhombic crystal structure with lattice parameters a=6.35 A°, b=3.74 A°, and c=3.64 A°. It is clear that as the W content increases, the XRD peaks are consistently shifted towards lower 2Θ values, meaning that the lattice is expanded as a function of W content. Specifically, the lattice parameters for 2.5% and 10% W are a=6.39 A°, b=3.8 A°, c=3.59 A°, and a=6.43 A°, b=3.83 A°, c=3.59 A°, respectively. This shows a lattice expansion in a and b directions. Knowing that the atomic radius of W is greater than that of Ta, we could refer the

lattice expansion to the incorporation of W. In fact, this tells us that W is preferably incorporated in planes that have projections in yz- and/or xz-planes such as (100), (010), (110), and (101). This is very useful when trying to model such system since it will help build a more realistic model and hence have more reliable information from the calculations. More importantly, it helps in designing more efficient nanotubular photoanodes for solar water splitting. This is because upon illumination, electrons are excited from the valence band of Ta_2O_5 to the conduction band of WO_3. Also it is known that charge separation should occur perpendicular to light absorption in order to attain high conversion efficiency and hence the nanotubes should be oriented such that the W-containing planes are aligned perpendicular to light absorption. In fact, that was the reason for low quantum efficiency in Ta_3N_5 nanotubular photoanodes as the nanotubes gets longer since the electrons have to travel for a longer distance till they reach the back contact which increases the probability of electron-hole recombination[109].

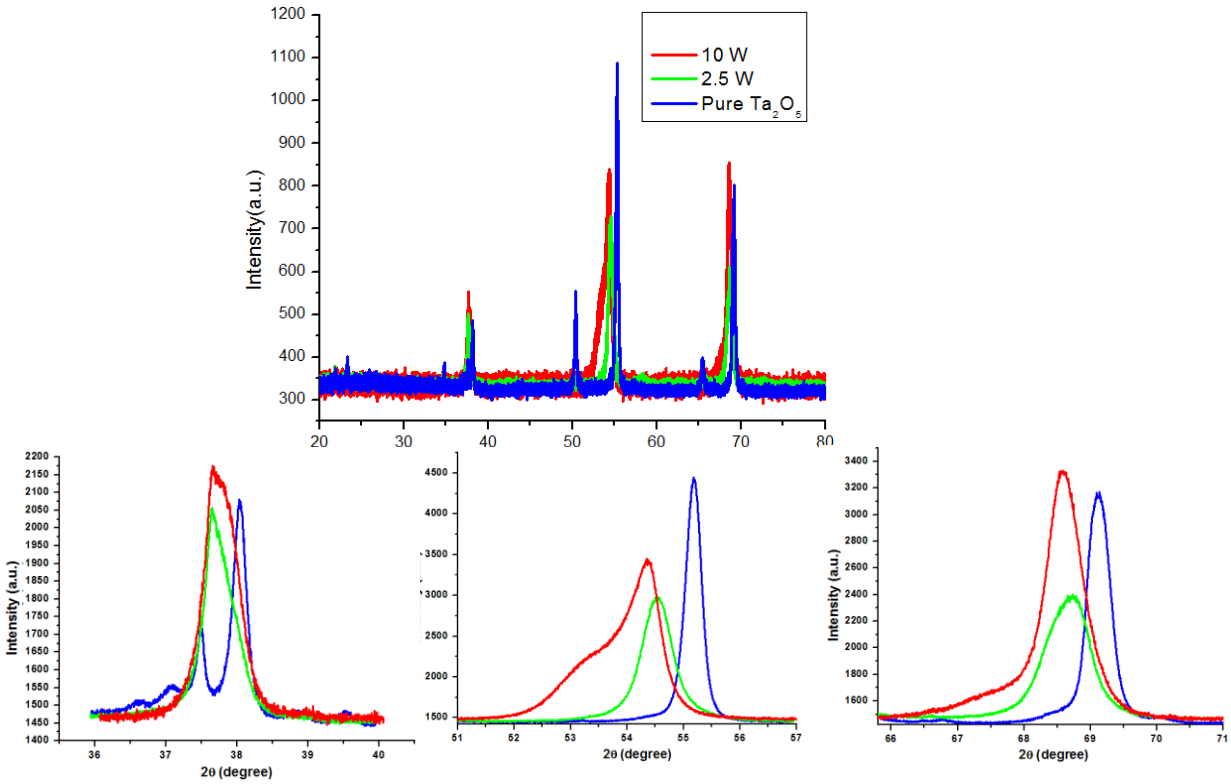

Figure 4.4: XRD pattern for pristine Ta2O5, 2.5%W, and 10%W, annealed for 4 hours

Figure 4.5 shows the XRD pattern for pristine and W-doped Ta_2O_5 for different annealing times. As the annealing time increases, the peaks are shifted towards larger 2Θ values indicating a contraction in the crystal lattice. This is because heating the lattice for longer times allows the atoms to readjust their positions, minimizing the total energy of the system. Also note that the extent peak shifting decreases as the W content increases. This is because W atom is larger than Ta and so it allows less space for the atoms to move in the lattice, decreasing the extent of freedom for readjustment.

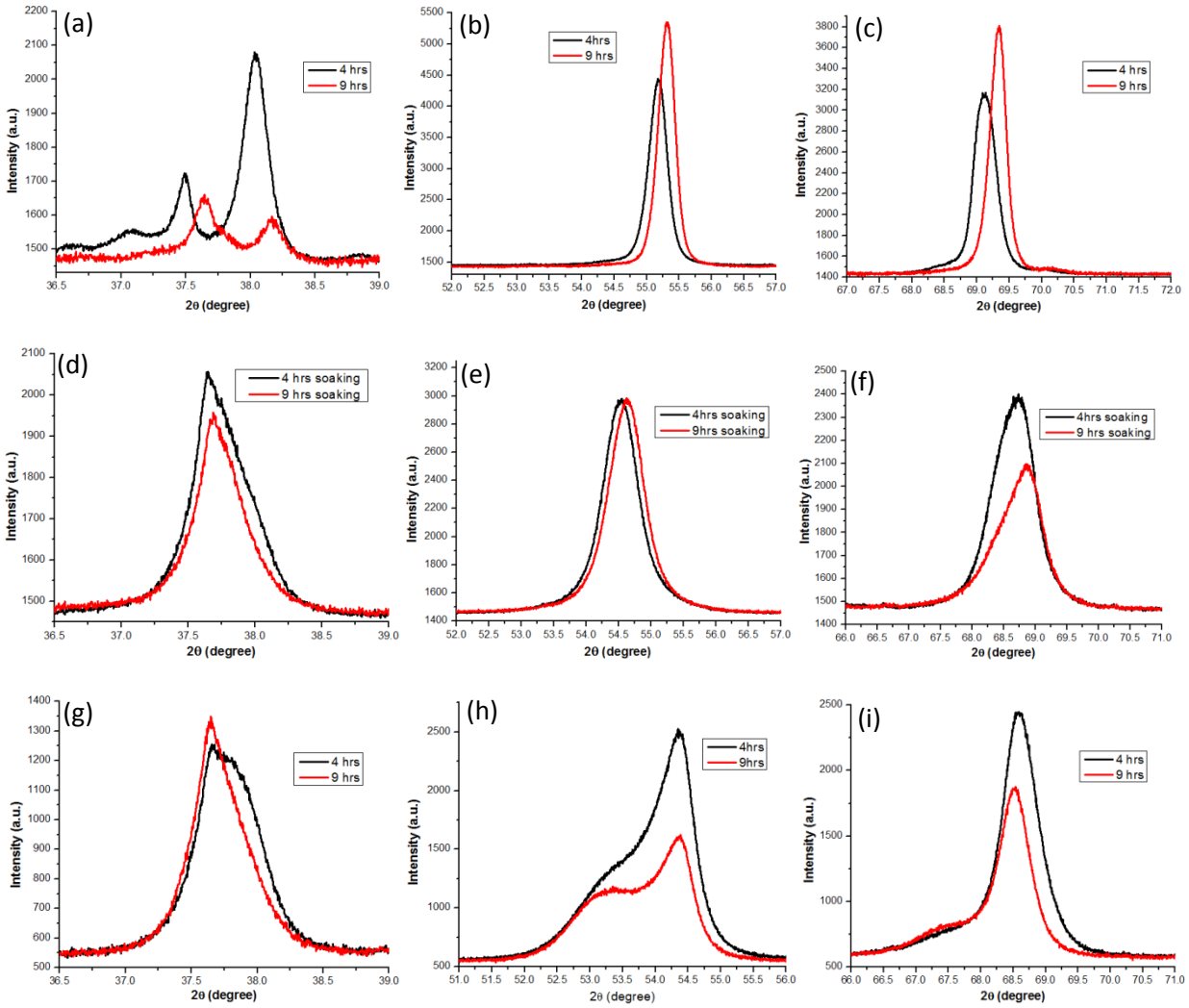

Figure 4.5: XRD pattern for pristine and W-doped Ta2O5 at 4 and 9 hours annealing. (a)-(c) Pristine Ta2O5, (d)-(f) 2.5% W, (g)-(i) 10%W.

4.3 X-Ray Photo-electron Spectroscopy (XPS)

In order to study the composition of the fabricated Ta_2O_5 and Ta-W-O nanotubes, XPS analysis was performed. The O1s peak was observed between 530.5 and 530.9 eV. This is in very good agreement with the O1s peak observed in Ta_2O_5 and WO_3 which lies between 530.3 and 530.8 eV. The shoulder in the O1s peak indicates the formation of Ta and /or W oxide. In pure Ta_2O_5, Ta4f peaks exist at 26.3 eV and 28.1 eV corresponding to 4f7/2 and 4f5/2 peaks respectively with a doublet separation of 1.8 eV which signifies the presence of Ta^{+5} state[110]. As the W

content increases to 2.5%, both the O1s peak as well as the Ta 4f peaks are shifted towards higher binding energy, indicating a decrease in the electron cloud around both oxygen and tantalum. This suggests an electron transfer from both O and Ta to W. This suggestion is asserted in Figure 4.6e which shows W 4f spectrum in which 4f7/2 and 4f5/2 peaks shift in opposite directions towards each other forming one peak instead of a doublet. The shift of 4f5/2 peak towards lower binding energy indicates an increase of the electron cloud around W which confirms the charge transfer from O and Ta to W. For 10%W, the O1s peak lies midway between that in pure Ta_2O_5 and 2.5%W case. Also the Ta4f peaks are shifted back towards lower binding energies. More interestingly, the W4f peaks are clearly deconvoluted into 4f7/2 and 4f5/2 peaks. However, the doublet separation is only 1.9 eV compared to 2.2 eV which is reported in the literature[111]. This deconvolution is a result of both 4f7/2 and 4f5/2 peaks moving apart from each other. The shift W 4f7/2 towards lower binding energy indicates a charge transfer from O to W. Note also that the shift of Ta 4f towards lower binding energy at 10%W indicates that some electrons are transferred from O to Ta.

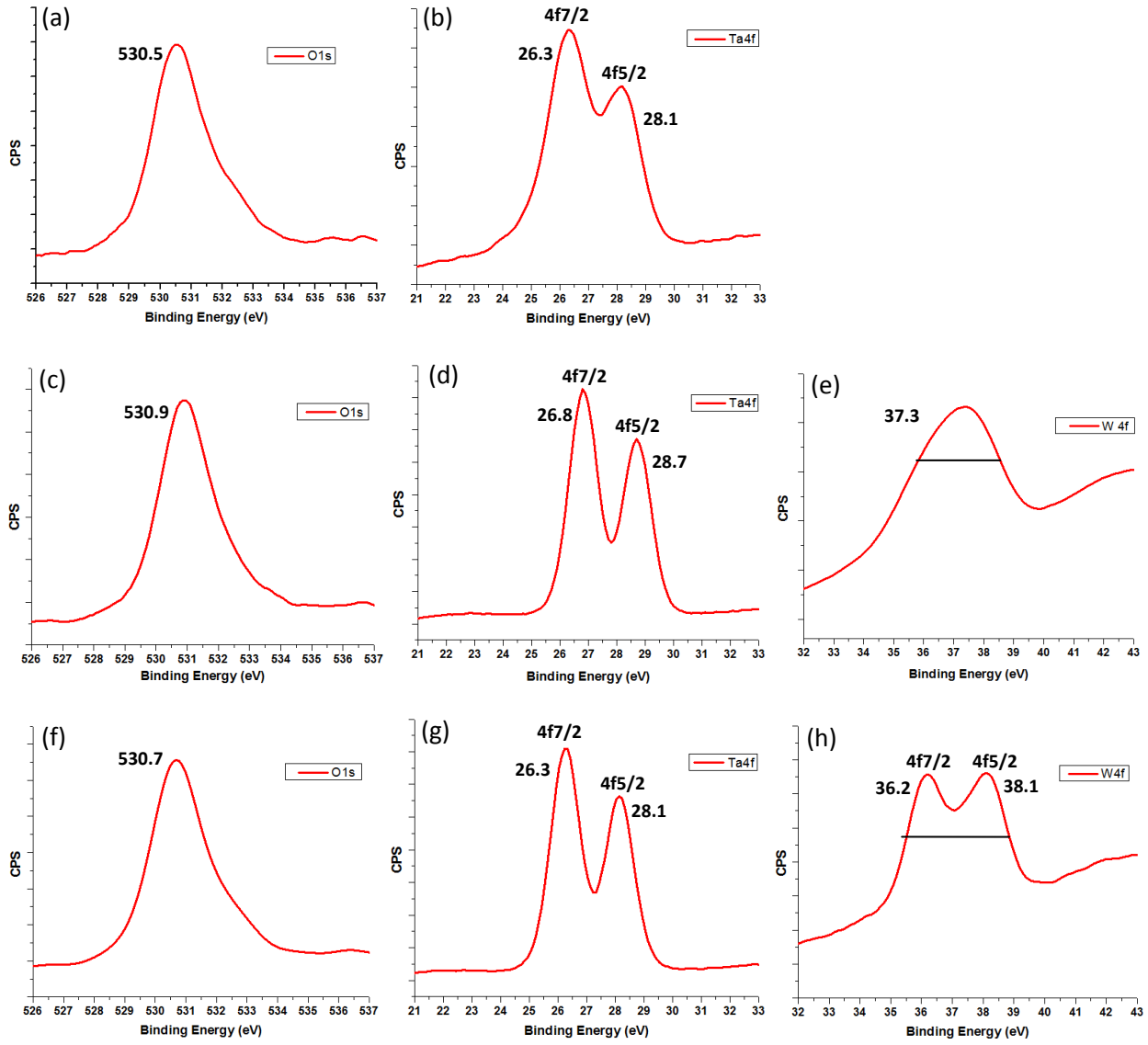

Figure 4.6: XPS analysis for (a) –(b)pure Ta2O5, (c)-(e)2.5%W, and (f)-(h)10%W

4.4 Diffuse Reflectance

Figure 4.7 shows the absorption spectrum of pure Ta_2O_5 as well as the W-doped Ta_2O_5. It is clear that as the W content increases, the absorption is red shifted corresponding to a decrease in the bandgap. This reduction in the bandgap is due to lowering of the conduction band edge since

it is well known that the conduction band of Ta_2O_5 is due to Ta 5d[60, 112] orbital and that W 5d is lower in energy than Ta 5d[113].

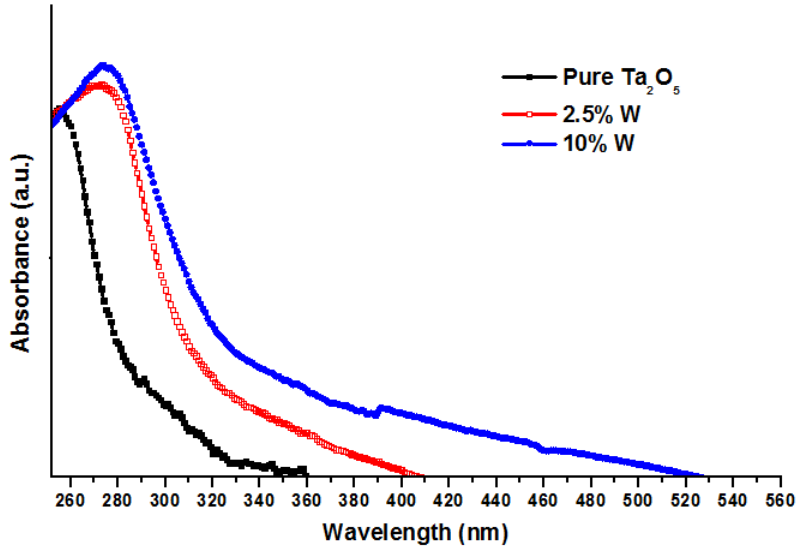

Figure 4.7: Diffuse reflectance spectra (DRS) for pure Ta_2O_5 and Ta–W-O nanotube electrodes annealed at 450°C for 9h in air.

Furthermore, there is an absorption tail which extends in the visible region as the content of W increases. This can be understood from the Crystal Field Theory where the W 5d orbitals are split into a set of filled orbitals occurring at a lower energy and another set of empty orbitals occurring at a higher energy as shown in Figure 4.8. The splitting occurs when a set of negative point charges move close to W atoms. The energy of some of the d-orbitals rises due to the repulsion between the d-oribtal electrons and the electrons approaching the W^{+6}. Each d-orbital is affected differently depending on the geometry of the surrounding negative charges, as shown in Figure 4.8. This asserts our assumption that upon illumination, the electrons are excited from the valence band of Ta_2O_5 to the conduction of WO_3. When the electrons are transferred towards WO_3, they increase the charge density around the W atoms causing the splitting of the d-orbitals. Figure 4.7 asserts that the extended absorption is mainly due to splitting of W 5d orbital and not Ta 5d because the absorption tail gets more extended as the amount of W increases.

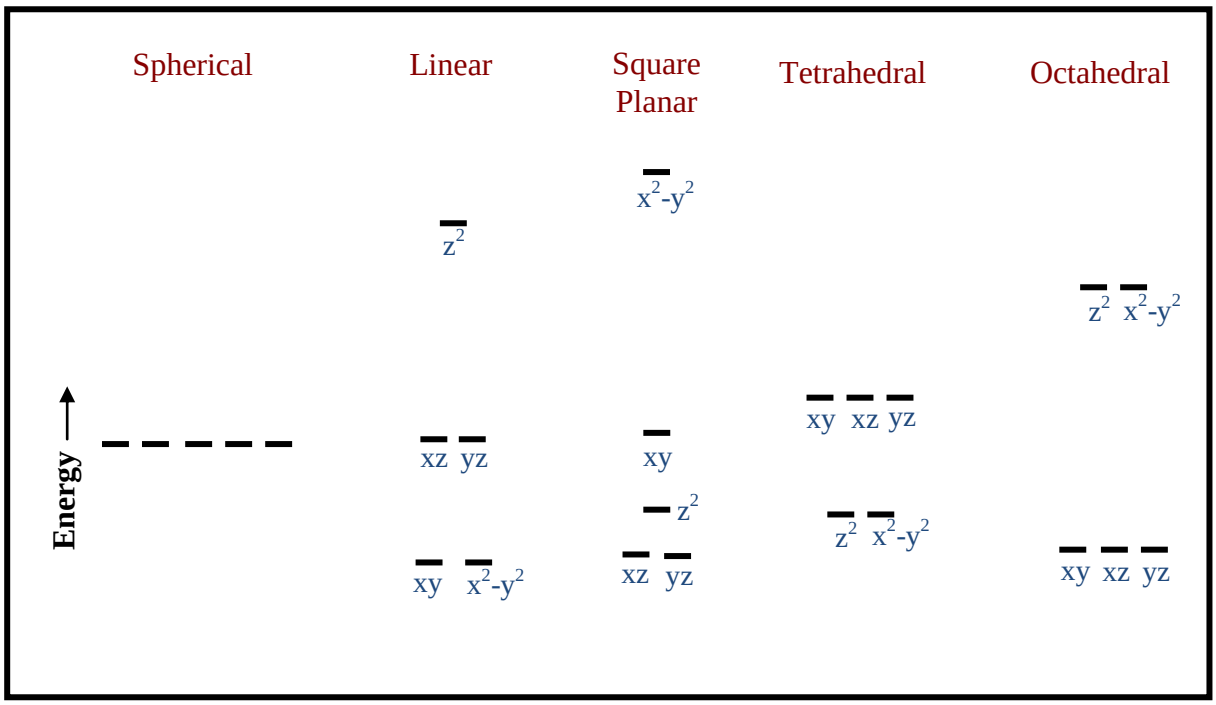

Figure 4.8: d-orbital splitting of metal ions and its dependence on the surrounding charge distribution

4.5 I-V Measurements

Figure 4.9 shows the photocurrent density versus the applied potential for pure Ta_2O_5 and Ta-W-O nanotubes. It is clear that the photocurrent increases by 100 times in going from pure Ta_2O_5 to 10%W alloy. The photocurrent increases monotonically as the W content increases. Furthermore, knowing that Ta-W-O system has an indirect bandgap[60], the length of the nanotubes is a significant factor in improving photon absorption since indirect bandgap materials have low absorption coefficients compared to their direct bandgap counterparts[114] and hence the optical path of light needs to be increased in order to increase the probability of photon absorption. This is asserted in Figure 4.9 where the photocurrent increases by more than five times with increasing the nanotube length of 10%W alloy from 0.5 μm to 1.4 μm. This is due to enhancement in photon absorption since the probability of photon absorption increases and hence

more photons are being absorbed which, in turn, increases the photocurrent. Moreover, the onset potential is shifted towards more negative values as the W content increases. This is because as the W content increases, the donor energy level is shifted more towards the conduction band edge which, in turn, shifts the Fermi level towards more negative potential. This is a desirable property since this open circuit potential represents the contribution of light towards the minimum potential difference required for water splitting (1.23 V)[7]. Table 4.1 summarizes the onset potential as well as the maximum photocurrent density for Ta_2O_5 and Ta-W-O nanotubes.

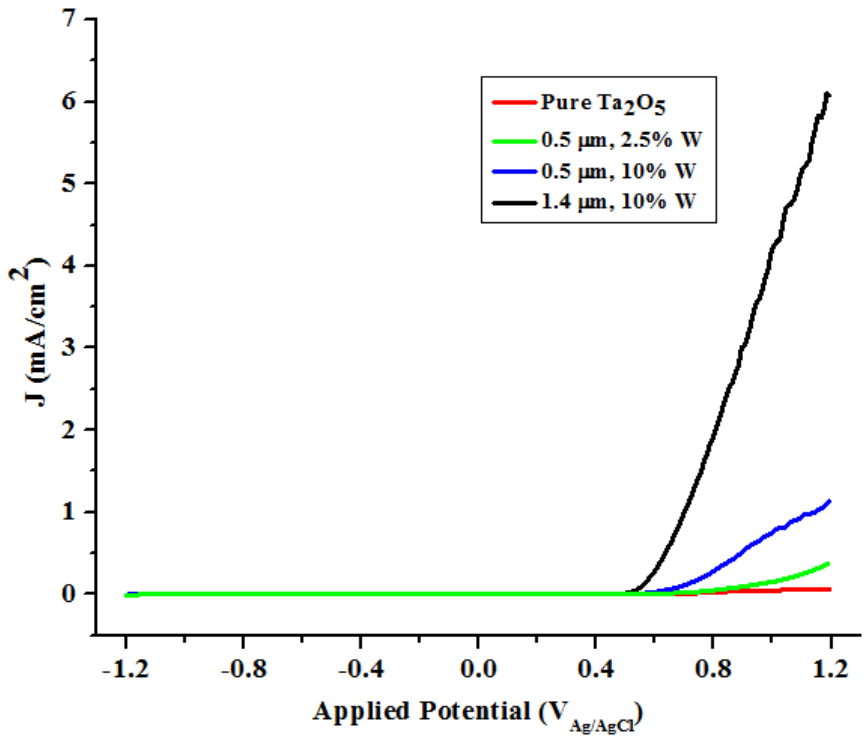

Figure 4.9: Photocurrent density vs potential in 1M KOH solution under AM1.5 illumination for pure Ta_2O_5 and Ta-W-O nanotubes

Table 4.4: Onset potential and maximum photocurrent for pure Ta_2O_5 and Ta-W-O nanotubes

	Onset Potential (V)	J_{max} (mA/cm^2)
Pure Ta_2O_5	-0.57	0.06
0.5 µm, 2.5% W	-1.025	0.38
0.5 µm, 10% W	-1.07	1.13
1.4 µm, 10% W	-1.06	6.08

CHAPTER 5

CONCLUSION AND FUTURE WORK

5.1 Conclusions

In this dissertation we studied the band structure and charge transfer properties of Ta-W-O system and the possibility of using it as a photoanode in photoelectrochemical water splitting system. We used Density Functional Theory in order to figure out the optimum W content that has optimum bandgap and charge carrier mobility. In order to do that, an accurate model for Ta_2O_5 crystal structure is required. All of Ta_2O_5 crystal structures proposed to date are not accurate enough since they cannot reproduce the practical bandgap. We found out that PBE0 hybrid functional is an efficient method for the bandgap estimation of Ta_2O_5. PBE0 showed better results compared to HSE06 due to the incorporation of HF exchange energy in short and long ranges, which allowed for a smaller self-interaction error. The calculated bandgap for δ-Ta_2O_5 under PBE0 calculation is 2.92 eV, which is the closest reported bandgap to experiment so far, suggesting that low-level computation can be used for qualitative analysis whereas high-level computation can be used whenever accurate results are required, at the expense of a more demanding computational power. We also proposed a new Ta_2O_5 orthorhombic structure. Using the PBE0 hybrid functional, this structure showed a bandgap energy of 3.7 eV, which is only 0.2 eV from the reported experimental value. The structure has a PMMM symmetry group with lattice constants a = 7.9 Å, and b = c = 3.75 Å. The computational time of our proposed structure is six times less than other reported structures under the same computational method, which allows for more detailed computations and hence investigation of more subtle properties of Ta_2O_5. We recommend this structure for further theoretical investigations and experimental verifications as it provides a minimum error in the calculated bandgap.

Based on our proposed structure, we calculated the band gap and the holes effective mass for Ta-W-O system. We chose the hole effective mass since the photoelectrochemical cell is a minority carrier device and the Ta-W-O alloy is an n-type semiconductor. We studied different alloy compositions with 8.3%, 25%, and 50% W content. We found that Ta-W-O semiconductor alloys have a widely tunable bandgap from 3.7 eV to 1 eV. The bandgap monotonically decreases with increasing the W content. The bandgap deviates from the linear composition dependency, showing a large composition-dependent bowing parameter. The bowing parameter at the different W content originates from different physical phenomena. At low W content, a high bowing parameter of -8.6 originates from charge exchange due to the interaction of the localized electron energy level in W with the extended states of the conduction band. The charge exchange decreases with increasing the W content due to the merging of the delocalized electron energy level in W with the extended states of the conduction band, decreasing the bowing parameter to -6.1 at 25% of W content. At 50%W, the bowing parameter increases again to -7.7 due to the volume change as observed by the XRD investigation. In fact, at W concentration higher than 10%, Ta_2O_5 and WO_3 tend to form microscopic heterostructures such that electrons are excited from the valence band of Ta_2O_5 to the conduction band of WO_3. The created electron-hole pair is well extracted due to the staggered bandgap nature of Ta-W-O alloy. Considering alloys such as Ti-Fe-O which suffer from excessive recombination due to the straddling bandgap nature, our results suggest that staggered bandgap would be desirable characteristics for efficient charge carrier separation. We also show that the effective mass of holes in pristine Ta_2O_5 as well as Ta-W-O alloys has minimum value along the y-direction. The effective mass in the y-direction monotonically decreases with increasing W content. At

sufficiently large W content (> 25 %), the effective mass is comparable to that of III-V semiconductors.

Based on the previous discussion, we recommend using 25% W system as a photoanode for water splitting since it has an optimum bandgap beside having an efficient charge separation because of the staggered bandgap effect. Furthermore, the hole effective mass at this W concentration is half that of pristine Ta_2O_5 and TiO_2, suggesting a large hole mobility and hence a minimum charge recombination. Of course, the practical feasibility of producing alloys with such high content of mixing ratio needs to be validated experimentally; however, the undertaken preliminary experiments show that it is possible to synthesize Ta-W-O alloys with W content up to 10% without severe problems. Furthermore, the analysis we already provided gives a good guidance on designing efficient active materials for water splitting systems as well as solar cells and points out some of the interesting phenomena that might occur for alloy systems at large mixing concentrations. We are currently extending this work to include the synthesis of larger W content Ta-W-O alloys. In fact, it turns out to be that this process becomes straight forward if we start with Ta-W alloys and then oxidize the alloy since W is totally soluble in Ta [115].

In order to test the efficiency of Ta-W-O system in water splitting, we investigated two alloys with a W content of 2.5% and 10%. We were unable to test higher concentrations due to time limitations. We were able to fabricate well-adhered nanotubes with controlled length, wall thickness, and diameter. We found out that the surface starts to crack after 4 minutes of anodization for pure Ta samples. For 2.5%W and 10%W samples, the surface cracks after 3 and 2.5 minutes respectively. The decrease in the maximum anodization time with increasing W content can be attributed to the stresses in the crystal lattice due to the substitution of some Ta atoms with W which caused the cracks to appear at earlier time. Optical and structure

characterizations were performed on the samples. Diffuse reflectance measurements show that as the W content increases, the absorption is red shifted corresponding to a decrease in the bandgap, which is caused due to lowering of the conduction band edge. Furthermore, there is an absorption tail which extends in the visible region as the content of W increases due to the splitting of W 5d orbitals. XPS measurements show that the O1s and Ta 4f peaks are shifted towards higher binding energy for 2.5%W alloy compared to pure Ta_2O_5, which suggests a charge transfer from O and Ta atoms to W atoms, in agreement with the charge transfer model derived from DFT. However, for 10%W, charge transfer is divided between Ta and W in which electrons are transferred from O atoms to both W and Ta atoms. This can be seen from the Ta4f and W 4f7/2 peaks being shifted towards lower binding energy, indicating an increase of charge density around Ta and W. Finally, I-V measurements show a 100x increase in the photocurrent in case of 10%W alloy as compared to pristine Ta_2O_5.

5.2 Future Work

Detailed DFT studies will be carried out on Ta-W-O system to understand its photocatalytic properties. Namely, the effect of point defects, such as oxygen vacancies, on the reactivity of Ta-W-O system will be considered. Secondly, spatial charge distribution will be calculated which should give strong, direct evidence on the origin of charge transfer and would help proof that electrons are excited from the valence band of Ta_2O_5 to the conduction band of WO_3. Furthermore, the effect of spatial distribution of W on the electronic and optical properties of the system will be studied. Moreover, the surface reactivity of the different Ta-W-O facets will be studied and the preferred surface for hydrogen production shall be determined. Also the effect of

other dopants, namely isovalent elements and rare-earth elements, on the structural and electronic properties of Ta_2O_5 will be studied and compared with Ta-W-O system.

On the practical side, higher W content alloys will be fabricated and their structural, electrical, and optical properties will be determined using XRD, XPS, diffuse reflectance, and photoelectrochemical techniques. Namely, 25% and 50%W alloys will be studied since they are expected to have promising optical properties as found from DFT simulations.

References

[1] P. D. Wurfel, *Physics of solar cells : from principles to new concepts*. Weinheim: Wiley-VCH, 2005.

[2] S. J. Hassol, *Impacts of a warming arctic : arctic climate impact assessment*. Cambridge: Cambridge University Press, 2004.

[3] C. D. Keeling, *et al.*, "Evolution of natural and anthropogenic fluxes of atmospheric CO2 from 1957 to 2003," *Tellus Series B-Chemical and Physical Meteorology,* vol. 63, pp. 1-22, Feb 2011.

[4] P. Brohan, *et al.*, "Uncertainty estimates in regional and global observed temperature changes: A new data set from 1850," *Journal of Geophysical Research-Atmospheres,* vol. 111, Jun 24 2006.

[5] N. S. Lewis, "Powering the planet," *Mrs Bulletin,* vol. 32, pp. 808-820, Oct 2007.

[6] I. P. Jain, "Hydrogen the fuel for 21st century," *International Journal of Hydrogen Energy,* vol. 34, pp. 7368-7378, Sep 2009.

[7] C. A. Grimes, *et al.*, *Light, water, hydrogen : the solar generation of hydrogen by water photoelectrolysis*. New York: Springer, 2008.

[8] A. J. Bard and M. A. Fox, "Artificial Photosynthesis - Solar Splitting of Water to Hydrogen and Oxygen," *Accounts of Chemical Research,* vol. 28, pp. 141-145, Mar 1995.

[9] A. J. Bard, "Design of Semiconductor Photo-Electrochemical Systems for Solar-Energy Conversion," *Journal of Physical Chemistry,* vol. 86, pp. 172-177, 1982.

[10] H. Gerischer, "On the stability of semiconductor electrodes against photodecomposition," *Journal of Electroanalytical Chemistry and Interfacial Electrochemistry,* vol. 82, pp. 133-143, 1977.

[11] A. J. Bard and L. R. Faulkner, *Electrochemical methods : fundamentals and applications*. New York: Wiley, 1980.

[12] N. Beermann, *et al.*, "Photoelectrochemical studies of oriented nanorod thin films of hematite," *Journal of the Electrochemical Society,* vol. 147, pp. 2456-2461, Jul 2000.

[13] A. Fujishima and K. Honda, "Electrochemical Photolysis of Water at a Semiconductor Electrode," *Nature,* vol. 238, pp. 37-38, 1972.

[14] O. Khaselev and J. A. Turner, "A monolithic photovoltaic-photoelectrochemical device for hydrogen production via water splitting," *Science,* vol. 280, pp. 425-427, Apr 17 1998.

[15] M. A. Butler, *et al.*, "Tungsten Trioxide as an Electrode for Photoelectrolysis of Water," *Solid State Communications,* vol. 19, pp. 1011-1014, 1976.

[16] A. Wolcott, *et al.*, "Photoelectrochemical Study of Nanostructured ZnO Thin Films for Hydrogen Generation from Water Splitting," *Advanced Functional Materials,* vol. 19, pp. 1849-1856, Jun 23 2009.

[17] D. Barreca, *et al.*, "The potential of supported Cu_2O and CuO nanosystems in photocatalytic H2 production," *ChemSusChem,* vol. 2, pp. 230-3, 2009.

[18] D. Chauhan, *et al.*, "Preparation and characterization of nanostructured CuO thin films for photoelectrochemical splitting of water," *Bulletin of Materials Science,* vol. 29, pp. 709-716, Dec 2006.

[19] A. J. Nozik, "Photoelectrolysis of Water Using Semiconducting TiO_2 Crystals," *Nature,* vol. 257, pp. 383-386, 1975.

[20] K. H. Yoon and D. J. Nam, "Photoelectrochemical Behavior of SnO_2 Thin-Film Electrodes Prepared by Ultrasonic Spray-Pyrolysis," *Journal of Materials Science,* vol. 30, pp. 3415-3420, Jul 1 1995.

[21] J. H. Park, *et al.*, "Novel carbon-doped TiO_2 nanotube arrays with high aspect ratios for efficient solar water splitting," *Nano Letters,* vol. 6, pp. 24-28, Jan 2006.

[22] R. Asahi, *et al.*, "Visible-light photocatalysis in nitrogen-doped titanium oxides," *Science,* vol. 293, pp. 269-271, Jul 13 2001.

[23] A. Ghicov, *et al.*, "Photoresponse in the visible range from Cr doped TiO_2 nanotubes," *Chemical Physics Letters,* vol. 433, pp. 323-326, Jan 12 2007.
[24] G. K. Mor, *et al.*, "Vertically oriented Ti-Fe-O nanotube array films: Toward a useful material architecture for solar spectrum water photoelectrolysis," *Nano Letters,* vol. 7, pp. 2356-2364, Aug 2007.
[25] N. K. Allam, *et al.*, "Vertically Oriented Ti-Pd Mixed Oxynitride Nanotube Arrays for Enhanced Photoelectrochemical Water Splitting," *Acs Nano,* vol. 5, pp. 5056-5066, Jun 2011.
[26] M. Radecka, *et al.*, "Photoelectrochemical properties of undoped and Ti-doped WO3," *Physica B-Condensed Matter,* vol. 364, pp. 85-92, Jul 15 2005.
[27] K. M. Karuppasamy and A. Subrahmanyam, "Results on the electrochromic and photocatalytic properties of vanadium doped tungsten oxide thin films prepared by reactive dc magnetron sputtering technique," *Journal of Physics D-Applied Physics,* vol. 41, Feb 7 2008.
[28] P. Maruthamuthu, *et al.*, "Hydrogen Evolution from Water with Visible Radiation in Presence of Cu(II)/WO_3 and Electron Relay," *International Journal of Hydrogen Energy,* vol. 14, pp. 525-528, 1989.
[29] A. J. Nozik, "Photoelectrochemistry - Applications to Solar-Energy Conversion," *Annual Review of Physical Chemistry,* vol. 29, pp. 189-222, 1978.
[30] G. R. Bamwenda and H. Arakawa, "The visible light induced photocatalytic activity of tungsten trioxide powders," *Applied Catalysis a-General,* vol. 210, pp. 181-191, Mar 9 2001.
[31] K. M. Karuppasamy and A. Subrahmanyam, "The electrochromic and photocatalytic properties of electron beam evaporated vanadium-doped tungsten oxide thin films," *Solar Energy Materials and Solar Cells,* vol. 92, pp. 1322-1326, Nov 2008.
[32] H. S. Park, *et al.*, "Factors in the Metal Doping of $BiVO_4$ for Improved Photoelectrocatalytic Activity as Studied by Scanning Electrochemical Microscopy and First-Principles Density-Functional Calculation," *Journal of Physical Chemistry C,* vol. 115, pp. 17870-17879, Sep 15 2011.
[33] S. Wilson, *Handbook of molecular physics and quantum chemistry*. Chichester: Wiley, 2003.
[34] J. M. Ziman, *Electrons and phonons : the theory of transport phenomena in solids*. Oxford: Clarendon Press, 1960.
[35] D. R. Hartree, "The wave mechanics of an atom with a non-Coulomb central field Part I theory and methods," *Proceedings of the Cambridge Philosophical Society,* vol. 24, pp. 89-110, Jul 1928.
[36] V. Fock, "Approximation method for the solution of the quantum mechanical multibody problems," *Zeitschrift für Physik,* vol. 61, pp. 126-148, Jan 1930.
[37] J. C. Slater, "Note on Hartree's method," *Physical Review,* vol. 35, pp. 0210-0211, Jan 1930.
[38] P. Hohenberg and W. Kohn, "Inhomogeneous Electron Gas," *Physical Review B,* vol. 136, pp. B864-&, 1964.
[39] L. H. Thomas, "The calculation of atomic fields.," *Proceedings of the Cambridge Philosophical Society,* vol. 23, pp. 542-548, Jul 1927.
[40] E. Fermi, "A statistical Method for Determining some Properties of the Atoms and its Application to the Theory of the periodic Table of Elements," *Zeitschrift für Physik,* vol. 48, pp. 73-79, Jan 1928.
[41] P. A. M. Dirac, "Note on exchange phenomena in the Thomas atom," *Proceedings of the Cambridge Philosophical Society,* vol. 26, pp. 376-385, Jul 1930.
[42] E. H. Lieb, "Thomas-Fermi and Related Theories of Atoms and Molecules," *Reviews of Modern Physics,* vol. 53, pp. 603-641, 1981.
[43] C. F. v. Weizsäcker, "Zur Theorie der Kernmassen," *Zeitschrift für Physik,* vol. 96, pp. 431-458, 1935/07/01 1935.
[44] J. L. Gazquez and E. V. Ludena, "The Weizsacker Term in Density Functional Theory,"

Chemical Physics Letters, vol. 83, pp. 145-148, 1981.
[45] W. Kohn and L. J. Sham, "Self-Consistent Equations Including Exchange and Correlation Effects," *Physical Review,* vol. 140, pp. 1133-&, 1965.
[46] K. Capelle, "A bird's-eye view of density-functional theory," *Brazilian Journal of Physics,* vol. 36, pp. 1318-1343, Dec 2006.
[47] J. C. Slater, "Atomic shielding constants," *Physical Review,* vol. 36, pp. 0057-0064, Jul 1930.
[48] E. Clementi, "AB INITIO COMPUTATIONS IN ATOMS AND MOLECULES," *Ibm Journal of Research and Development,* vol. 9, pp. 2-&, 1965.
[49] W. Koch and M. C. Holthausen, *A chemist's guide to density functional theory / Wolfram Koch, Max C. Holthausen*: Weinheim ; New York : Wiley-VCH, c2001.
2nd ed., 2001.
[50] D. M. Ceperley and B. J. Alder, "GROUND-STATE OF THE ELECTRON-GAS BY A STOCHASTIC METHOD," *Physical Review Letters,* vol. 45, pp. 566-569, 1980.
[51] J. P. Perdew*, et al.*, "Generalized gradient approximation made simple," *Physical Review Letters,* vol. 77, pp. 3865-3868, Oct 1996.
[52] A. D. Becke, "DENSITY-FUNCTIONAL EXCHANGE-ENERGY APPROXIMATION WITH CORRECT ASYMPTOTIC-BEHAVIOR," *Physical Review A,* vol. 38, pp. 3098-3100, Sep 1988.
[53] C. T. Lee*, et al.*, "DEVELOPMENT OF THE COLLE-SALVETTI CORRELATION-ENERGY FORMULA INTO A FUNCTIONAL OF THE ELECTRON-DENSITY," *Physical Review B,* vol. 37, pp. 785-789, Jan 1988.
[54] J. P. Perdew*, et al.*, "Accurate density functional with correct formal properties: A step beyond the generalized gradient approximation," *Physical Review Letters,* vol. 82, pp. 2544-2547, Mar 1999.
[55] A. D. Becke, "Density-functional thermochemistry," *Abstracts of Papers of the American Chemical Society,* vol. 212, pp. 112-COMP, Aug 1996.
[56] J. M. Tao*, et al.*, "Climbing the density functional ladder: Nonempirical meta-generalized gradient approximation designed for molecules and solids," *Physical Review Letters,* vol. 91, Oct 2003.
[57] O. Gunnarsson and B. I. Lundqvist, "EXCHANGE AND CORRELATION IN ATOMS, MOLECULES, AND SOLIDS BY SPIN-DENSITY FUNCTIONAL FORMALISM," *Physical Review B,* vol. 13, pp. 4274-4298, 1976.
[58] A. D. Becke, "DENSITY-FUNCTIONAL THERMOCHEMISTRY .3. THE ROLE OF EXACT EXCHANGE," *Journal of Chemical Physics,* vol. 98, pp. 5648-5652, Apr 1993.
[59] N. Ndiege*, et al.*, "Synthesis, Characterization, and Photoactivity of Ta2O5-Grafted SiO2 Nanoparticles," *Chemistry – A European Journal,* vol. 17, pp. 7685-7693, 2011.
[60] R. Nashed*, et al.*, "Unravelling the interplay of crystal structure and electronic band structure of tantalum oxide (Ta_2O_5)," *Physical Chemistry Chemical Physics,* vol. 15, pp. 1352-1357, 2013.
[61] H. J. Monkhorst and J. D. Pack, "Special Points for Brillouin-Zone Integrations," *Physical Review B,* vol. 13, pp. 5188-5192, 1976.
[62] J. S. Lin*, et al.*, "Optimized and Transferable Nonlocal Separable Abinitio Pseudopotentials," *Physical Review B,* vol. 47, pp. 4174-4180, Feb 15 1993.
[63] D. Vanderbilt, "Soft Self-Consistent Pseudopotentials in a Generalized Eigenvalue Formalism," *Physical Review B,* vol. 41, pp. 7892-7895, Apr 15 1990.
[64] Stephens.Nc and R. S. Roth, "STRUCTURAL SYSTEMATICS IN BINARY SYSTEM TA_2O_5-WO_3. .5. STRUCTURE OF LOW-TEMPERATURE FORM OF TANTALUM OXIDE L-TA2O5," *Acta Crystallographica Section B-Structural Crystallography and Crystal Chemistry,* vol. B 27, pp. 1037-&, 1971.
[65] L. A. Aleshina and S. V. Loginova, "Rietveld analysis of X-ray diffraction pattern from beta-Ta2O5 oxide," *Crystallography Reports,* vol. 47, pp. 415-419, May-Jun 2002.
[66] M. Hiratani*, et al.*, "Hexagonal polymorph of tantalum-pentoxide with enhanced dielectric constant," *Applied Physics Letters,* vol. 81, pp. 2433-2435, Sep 23 2002.

[67] H. Fujikawa and Y. Taga, "Effects of Additive Elements on Electrical-Properties of Tantalum Oxide-Films," *Journal of Applied Physics,* vol. 75, pp. 2538-2544, Mar 1 1994.
[68] N. Terao, "Structure des Oxides de Tantale," *Japanese Journal of Applied Physics,* vol. 6, p. 21.
[69] B. Tamamushi*, et al.*, *Iwanami rikagaku jiten*, 1981.
[70] A. Fukumoto and K. Miwa, "Prediction of hexagonal Ta2O5 structure by first-principles calculations," *Physical Review B,* vol. 55, pp. 11155-11160, May 1 1997.
[71] T. K. Gu*, et al.*, "First-principles simulations on bulk Ta2O5 and Cu/Ta_2O_5/Pt heterojunction: Electronic structures and transport properties," *Journal of Applied Physics,* vol. 106, Nov 15 2009.
[72] B. R. Sahu and L. Kleinman, "Theoretical study of structural and electronic properties of beta-Ta2O5 and delta-Ta2O5," *Physical Review B,* vol. 69, Apr 2004.
[73] W. Andreoni and C. A. Pignedoli, "Ta_2O_5 polymorphs: Structural motifs and dielectric constant from first principles," *Applied Physics Letters,* vol. 96, Feb 8 2010.
[74] S. Lagergren and A. Magneli, "On the Tantalum Oxygen System," *Acta Chemica Scandinavica,* vol. 6, pp. 444-446, 1952.
[75] A. I. Zaslavskii*, et al.*, "Rentgenograficheskoe Issledovanie Polimorfizma Ta2o5," *Doklady Akademii Nauk Sssr,* vol. 104, pp. 409-411, 1955.
[76] F. Laves and W. Petter, "Eine Displazive Umwandlung Bei Alpha-Ta_2O_5," *Helvetica Physica Acta,* vol. 37, pp. 617-&, 1964.
[77] Y. N. Wu*, et al.*, "First-principles studies of Ta_2O_5 polymorphs," *Physical Review B,* vol. 83, Apr 2011.
[78] K. M. Parida*, et al.*, "Fabrication of NiO/Ta_2O_5 composite photocatalyst for hydrogen production under visible light," *International Journal of Energy Research,* vol. 37, pp. 161-170, Feb 2013.
[79] M. Stodolny and M. Laniecki, "Synthesis and characterization of mesoporous Ta_2O_5-TiO_2 photocatalysts for water splitting," *Catalysis Today,* vol. 142, pp. 314-319, Apr 2009.
[80] W. J. Chun*, et al.*, "Conduction and valence band positions of Ta_2O_5, TaON, and Ta_3N_5 by UPS and electrochemical methods," *Journal of Physical Chemistry B,* vol. 107, pp. 1798-1803, Feb 2003.
[81] S. Agrawal*, et al.*, "First-principles study of the excited-state properties of coumarin-derived dyes in dye-sensitized solar cells," *Journal of Materials Chemistry,* vol. 21, pp. 11101-11108, 2011.
[82] J. B. Li and L. W. Wang, "Band-structure-corrected local density approximation study of semiconductor quantum dots and wires," *Physical Review B,* vol. 72, Sep 2005.
[83] M. V. Ivanov*, et al.*, "Electronic structure of delta-Ta_2O_5 with oxygen vacancy: ab initio calculations and comparison with experiment," *Journal of Applied Physics,* vol. 110, Jul 2011.
[84] J. Heyd*, et al.*, "Hybrid functionals based on a screened Coulomb potential," *Journal of Chemical Physics,* vol. 118, pp. 8207-8215, May 2003.
[85] J. Heyd*, et al.*, "Hybrid functionals based on a screened Coulomb potential (vol 118, pg 8207, 2003)," *Journal of Chemical Physics,* vol. 124, Jun 2006.
[86] S. Boughaba*, et al.*, "Synthesis of tantalum pentoxide films by pulsed laser deposition: material characterization and scale-up," *Thin Solid Films,* vol. 358, pp. 104-113, Jan 10 2000.
[87] M. Pastore*, et al.*, "A Computational Investigation of Organic Dyes for Dye-Sensitized Solar Cells: Benchmark, Strategies, and Open Issues," *Journal of Physical Chemistry C,* vol. 114, pp. 7205-7212, Apr 22 2010.
[88] H. Kominami*, et al.*, "Solvothermal synthesis of tantalum(V) oxide nanoparticles and their photocatalytic activities in aqueous suspension systems," *Physical Chemistry Chemical Physics,* vol. 3, pp. 2697-2703, 2001.
[89] J. N. Kondo*, et al.*, "Synthesis and property of mesoporous tantalum oxides," *Topics in*

Catalysis, vol. 19, pp. 171-177, 2002.
[90] J. M. Ngaruiya*, et al.*, "Preparation and characterization of tantalum oxide films produced by reactive DC magnetron sputtering," *Physica Status Solidi a-Applications and Materials Science,* vol. 198, pp. 99-110, Jul 2003.
[91] N. K. Allam*, et al.*, "Self-Assembled Fabrication of Vertically Oriented Ta_2O_5 Nanotube Arrays, and Membranes Thereof, by One-Step Tantalum Anodization," *Chemistry of Materials,* vol. 20, pp. 6477-6481, 2008/10/28 2008.
[92] J. Heyd*, et al.*, "Energy band gaps and lattice parameters evaluated with the Heyd-Scuseria-Ernzerhof screened hybrid functional," *Journal of Chemical Physics,* vol. 123, Nov 2005.
[93] J. Heyd and G. E. Scuseria, "Assessment and validation of a screened Coulomb hybrid density functional," *Journal of Chemical Physics,* vol. 120, pp. 7274-7280, Apr 2004.
[94] J. Jaramillo*, et al.*, "Local hybrid functionals," *Journal of Chemical Physics,* vol. 118, pp. 1068-1073, Jan 2003.
[95] A. V. Krukau*, et al.*, "Influence of the exchange screening parameter on the performance of screened hybrid functionals," *Journal of Chemical Physics,* vol. 125, Dec 2006.
[96] J. Paier*, et al.*, "Screened hybrid density functionals applied to solids," *Journal of Chemical Physics,* vol. 124, Apr 2006.
[97] S. Kakio*, et al.*, "Surface Acoustic Wave Properties of Amorphous Ta_2O_5 and Nb_2O_5 Thin Films Prepared by Radio Frequency Sputtering," *Japanese Journal of Applied Physics,* vol. 51, Jul 2012.
[98] F. Wang*, et al.*, "Doping of WO_3 for Photocatalytic Water Splitting: Hints from Density Functional Theory," *The Journal of Physical Chemistry C,* vol. 116, pp. 8901-8909, 2012/04/26 2012.
[99] M. V. Ivanov*, et al.*, "Electronic structure of delta -Ta_2O_5 with oxygen vacancy: ab initio calculations and comparison with experiment," *Journal of Applied Physics,* vol. 110, p. 024115, 2011.
[100] T. Gu*, et al.*, "First-principles simulations on bulk Ta_2O_5 and Cu/Ta_2O_5/Pt heterojunction: Electronic structures and transport properties," *Journal of Applied Physics,* vol. 106, p. 103713, 2009.
[101] W. J. Yin*, et al.*, "Band structure engineering of semiconductors for enhanced photoelectrochemical water splitting: The case of TiO_2," *Physical Review B,* vol. 82, Jul 12 2010.
[102] E. Thimsen*, et al.*, "Predicting the Band Structure of Mixed Transition Metal Oxides: Theory and Experiment," *Journal of Physical Chemistry C,* vol. 113, pp. 2014-2021, Feb 5 2009.
[103] J. E. Bernard and A. Zunger, "Electronic-Structure of ZnS, ZnSe, ZnTe, and Their Pseudobinary Alloys," *Physical Review B,* vol. 36, pp. 3199-3228, Aug 15 1987.
[104] S. H. Wei and A. Zunger, "Giant and composition-dependent optical bowing coefficient in GaAsN alloys," *Physical Review Letters,* vol. 76, pp. 664-667, Jan 22 1996.
[105] J. M. Ziman, *Principles of the theory of solids*, 2d ed. Cambridge Eng.: University Press, 1972.
[106] B. Enright and D. Fitzmaurice, "Spectroscopic Determination of Electron and Hole Effective Masses in a Nanocrystalline Semiconductor Film," *The Journal of Physical Chemistry,* vol. 100, pp. 1027-1035, 1996/01/01 1996.
[107] H. A. El-Sayed and V. I. Birss, "Controlled Interconversion of Nanoarray of Ta Dimples and High Aspect Ratio Ta Oxide Nanotubes," *Nano Letters,* vol. 9, pp. 1350-1355, 2009/04/08 2009.
[108] H. A. El-Sayed*, et al.*, "New insights into the initial stages of Ta oxide nanotube formation on polycrystalline Ta electrodes," *Nanoscale,* vol. 5, pp. 1494-1498, 2013.
[109] X. J. Feng*, et al.*, "Ta3N5 Nanotube Arrays for Visible Light Water Photoelectrolysis," *Nano Letters,* vol. 10, pp. 948-952, Mar 2010.

[110] F. Kurnia, *et al.*, "Composition dependence of unipolar resistance switching in TaOx thin films," *physica status solidi (RRL) – Rapid Research Letters,* vol. 5, pp. 253-255, 2011.
[111] G. P. Halada and C. R. Clayton, "Comparison of Mo--N and W--N synergism during passivation of stainless steel through x-ray photoelectron spectroscopy and electrochemical analysis," 1993, pp. 2342-2347.
[112] Y.-N. Wu, *et al.*, "First-principles studies of Ta_2O_5 polymorphs," *Physical Review B,* vol. 83, p. 144105, 2011.
[113] A. J. Nozik, "Photoelectrochemistry: Applications to Solar Energy Conversion," *Annual Review of Physical Chemistry,* vol. 29, pp. 189-222, 1978.
[114] B. G. Yacobi, *Semiconductor materials : an introduction to basic principles*. New York: Kluwer Academic/Plenum Publishers, 2003.
[115] T. B. Massalski and H. Okamoto, *Binary alloy phase diagrams*, 2nd ed. ed. Materials Park, Ohio: ASM International, 1990.